Published online 9 August 2017 *Nucleic Acids Research, 2017, Vol. 45, No. 18* ***10649–10671***
doi: 10.1093/nar/gkx709

Nucleic acid binding proteins affect the subcellular distribution of phosphorothioate antisense oligonucleotides

Jeffrey K. Bailey, Wen Shen*, Xue-hai Liang and Stanley T. Crooke

Department of Core Antisense Research, Ionis Pharmaceuticals, Inc. 2855 Gazelle Court, Carlsbad, CA 92010, USA

Received February 08, 2017; Revised July 10, 2017; Editorial Decision August 02, 2017; Accepted August 04, 2017

ABSTRACT

Antisense oligonucleotides (ASOs) are versatile tools that can regulate multiple steps of RNA biogenesis in cells and living organisms. Significant improvements in delivery, potency, and stability have been achieved through modifications within the oligonucleotide backbone, sugar and heterocycles. However, these modifications can profoundly affect interactions between ASOs and intracellular proteins in ways that are only beginning to be understood. Here, we report that ASOs with specific backbone and sugar modifications can become localized to cytoplasmic ribonucleoprotein granules such as stress granules and those seeded by the aggregation of specific ASO-binding proteins such as FUS/TLS (FUS) and PSF/SFPQ (PSF). Further investigation into the basis for ASO-FUS binding illustrated the importance of ASO backbone and hydrophobic 2′ sugar modifications and revealed that the C-terminal region of FUS is sufficient to retain ASOs in cellular foci. Taken together, the results of this study demonstrate that affinities of various nucleic acid binding domains for ASO depend on chemical modifications and further demonstrate how ASO–protein interactions influence the localization of ASOs.

INTRODUCTION

ASOs are short nucleic acid polymers designed to hybridize with and modulate the functions of specific cellular RNAs (1–3). ASOs are used in basic research and as therapeutics to target RNAs for RNase H1-mediated cleavage and degradation (4) and can also be designed to affect aspects of RNA processing such as RNA splicing (5–8) and polyadenylation (9–11) or mRNA translation (12,13). Incorporation of various chemical modifications within the polymer backbone, the sugar or the nucleobases substantially influences the antisense mechanism engaged upon ASO binding to its target RNA (14). RNase H1-dependent ASOs are usually designed as full phosphorothioate (PS) 'gapmers' consisting of a central deoxynucleotide gap (to support RNA strand cleavage by RNase H1) flanked by 2′-ribose-modified nucleotides (known as 'wings') to enhance ASO affinity for the target RNA and increase ASO nuclease stability. Chemical modifications have also been designed to influence the protein binding and tissue distribution profile of ASOs when administered *in vivo* (15–18). The 2′ modifications currently used in clinical and preclinical phosphorothioate antisense oligonucleotides (PS-ASOs) include: 2′-*O*-methoxyethyl (MOE), 2′-*O*-methyl (OMe), 2′-fluoro (F), 2′4′-locked nucleic acid (LNA), and 2′,4′-constrained 2′-*O*-ethyl (cEt) (14). Each MOE or OMe modification increases the melting temperature of an ASO–RNA duplex by 0.5–1°C, whereas F and 2′4'-bridged nucleic acids such as LNA and cEt stabilize duplex interactions to a greater extent (1–2.5°C per modification for F and 3–5°C per modification for LNA and cEt) (14,19–21). Although the reduction in RNA target levels *in vitro* mediated by ASOs is usually correlated with RNA affinity provided by these 2′ modifications (16,19,22), the correlation is strongest for ASOs with intermediate duplex melting temperatures (55–80°C), suggesting that factors other than RNA affinity contribute to ASO activity (16).

A hybridization-independent factor that contributes to the efficacy of ASOs *in vitro* and *in vivo* is interactions with proteins. In animals, ASOs with phosphodiester (PO) or charge-neutral backbones (such as peptide nucleic acids and morpholinos) dosed parenterally are rapidly excreted without significant tissue absorption (15). In contrast, ASOs with phosphorothioate (PS) backbones are highly bound (>90%) by plasma proteins and cell membrane proteins resulting in systemic distribution and ultimate uptake of the drugs into tissues and cells (15,23,24). In addition, binding of PS-ASOs with intracellular proteins influences subcellular distribution and antisense activity of PS-ASOs. At least 50 intracellular proteins have been identified that bind PS-ASOs (25–30). The 2′ modifications and oligonucleotide structures also influence PS-ASO–protein interactions (18,28,31,32). For example, heat shock protein 90 (Hsp90) preferentially binds to and enhances the

*To whom correspondence should be addressed. Tel: +1 760 603 2482; Fax: +1 760 603 4561; Email: wshen@ionisph.com

activity of cEt-modified PS-ASOs compared with MOE PS-ASOs (28). Moreover, the levels of paraspeckle proteins non-POU domain-containing octamer-binding protein (NONO/P54nrb) and splicing factor, proline- and glutamine-rich (SFPQ/PSF) are rapidly reduced by F-modified PS-ASOs but not by sequence-matched PS-ASOs modified with MOE, cET or LNA (32). Furthermore, the ASO sequence also influences interaction of PS-ASOs with specific proteins. For example, the affinity of the PS-ASO binding protein P54nrb differed by 100-fold for 12 different 3–10–3 cEt gapmer PS-ASO sequences (31). Such findings indicate that a deeper understanding of ASO–protein interactions is needed to inform future ASO design efforts.

Here, we report that 5–10–5 gapmer PS-ASOs localized to a variety of cytoplasmic ribonucleoprotein (RNP) granules, including cytoplasmic stress granules and RNP granules formed by mutant isoforms of Translocated in Liposarcoma/Fused in Sarcoma (TLS/FUS) and PSF, two ubiquitously expressed nuclear proteins with roles in RNA splicing, transcription and other aspects of RNA metabolism (33–36). Cytoplasmic stress granules are dynamic messenger ribonucleoprotein (mRNP) particles formed from stalled translation initiation complexes in response to environmental stress (37–39). In some patients with amyotrophic lateral sclerosis (ALS) or frontotemporal lobar degeneration (FTLD), FUS and PSF are partially excluded from the nucleus and seed the formation of cytoplasmic RNP granules that are similar to yet distinct from stress granules (36,40–44). Indeed, many disease-linked FUS mutations disrupt a nuclear localization signal (NLS) within the FUS C-terminus and are sufficient to cause cytoplasmic accumulation and subsequent aggregation of NLS-mutant FUS in cultured cells and transgenic animal models (33,40,45–48). Like stress granules, FUS granules are positive for some of the same marker proteins including Ras GTPase-activating protein-Binding Protein 1 (G3BP) and T cell Intracellular Antigen-1 cytotoxic granule-associated RNA binding protein-like 1 (TIAR) (36). However, endogenous, non-mutated FUS is only recruited to stress granules formed in response to osmotic stress (36,49), and FUS granules formed by ectopic expression of NLS-mutant FUS exhibit different assembly kinetics, morphology, reduced docking with P-bodies, and some differences in protein composition compared with canonical stress granules (43). The precise mechanistic link between FUS, stress granule dynamics and neurodegenerative disease remains a topic of active investigation (36,40,44).

We found that the amount of PS-ASO localized to FUS granules was affected by 2′ sugar modification. The cEt-modified PS-ASOs displayed approximately 2-fold greater granule enrichment than 2′ MOE, F or DNA PS-ASO of the same sequence. To characterize this effect, we used a recently developed bioluminescence resonance energy transfer (BRET) assay for nucleic acid-protein interactions to examine in detail the contribution of 2′ modifications and backbone chemistry to PS-ASO binding to specific domains of FUS *in vitro*. We discovered that FUS contains at least two high affinity (K_D < 50 nM) PS-ASO binding sites, one of which is sufficient to recruit cEt PS-ASO to artificial beta-sheet aggregates in the cell cytoplasm. These data support the hypothesis that high affinity interactions with nucleic acid binding proteins can affect the subcellular distribution of PS-ASOs and extend our understanding of the influence of various proteins on PS-ASO behaviors in cells.

MATERIALS AND METHODS

Reagents

Unless otherwise specified, all reagents/materials were purchased from VWR, Thermo Fisher Scientific or Sigma-Aldrich.

Plasmid construction, primers and ASO sequences

Sequence details can be found in the supplementary tables: plasmid construction, Supplementary Table S1; cloning primers, Supplementary Table S2; gBlock synthetic DNA templates, Supplementary Table S3; and ASO sequences and chemical modifications, Supplementary Table S4. Plasmids were confirmed by restriction digest and sequencing.

Antibodies

Primary antibodies used for western blotting (WB) or immunocytochemistry (ICC) are as follows: mouse anti-FLAG (Sigma-Aldrich F1804, WB 1:3000), mouse anti-G3BP (Abcam ab56574, ICC 1:600), rabbit anti-HA (Abcam ab9110, WB 1:4000, ICC 1:300), mouse anti-tGFP (OriGene TA150041, WB: 1:1000), mouse anti-GAPDH (Santa Cruz Biotechnology sc32233, WB: 1:1000), mouse anti-FUS (Santa Cruz Biotechnology sc47711, WB: 1:1000), mouse anti-PSF (Santa Cruz Biotechnology sc374502, WB: 1:1000), rabbit anti-mono-methyl arginine (Cell Signaling Technology 8015, WB: 1:1000), and rabbit anti-dimethyl arginine, asymmetric (EMD Millipore 07-414, WB: 1:1000). Secondary antibodies used for western blotting or immunocytochemistry are as follows: goat anti-rabbit IgG (H+L)-HRP (Bio-Rad 1706515, WB 1:2000), goat anti-mouse IgG (H+L)-HRP (Bio-Rad 1706516, WB 1:2000), goat anti-rabbit IgG (H+L)-AlexaFluor488 (Jackson ImmunoResearch 111-545-144, ICC 1:200), goat anti-rabbit IgG (H+L)-Cy5 (Jackson ImmunoResearch 111-175-144, ICC 1:200), goat anti-mouse IgG (H+L)-AlexaFluor488 (Jackson ImmunoResearch 115-545-146, ICC 1:200), and goat anti-mouse IgG (H+L)-Cy5 (Jackson ImmunoResearch 115-175-146, ICC 1:200).

Cell culture, transfection of ASOs and plasmids

HeLa, A431 and Lenti-X 293T (Clontech) cells were cultured in Dulbecco's Modified Eagle Medium (DMEM) supplemented with 10% fetal bovine serum (FBS) and 1× penicillin–streptomycin (Thermo Fisher Scientific) as described previously (29). Cells were passaged using 0.25% Trypsin–EDTA and seeded at approximately 1.25×10^4 cells/cm^2 onto either sterile 12-mm collagen-coated #1.5 glass coverslips (GG-12-1.5-collagen, Neuvitro Corporation) or 35-mm collagen-coated live imaging dishes (P35GCOL-1.5-14-C, MatTek). For ASO transfections, cells were washed once with 1× PBS and incubated for 4–6 h in Opti-MEM medium with a final concentration of 50 nM ASO and 4 μg/ml Lipofectamine 2000 (Thermo Fisher

Scientific). For plasmid transfections, DNA and TurboFect transfection reagent (Thermo Fisher Scientific) were mixed in Opti-MEM, incubated for 15 min at room temperature, and added to cell culture medium for 16–24 h according to the manufacturer's instructions. Culture vessels for Lenti-X293T cells were coated with 1:500 Matrigel (Corning) in serum-free DMEM for 4–6 h at 37°C prior to use.

Stress granule induction and electroporation of PS-ASOs

For stress granule induction, cells were lipid-transfected with ASO for 4 h (as described above) followed by a 1-h incubation with either 0.1% DMSO vehicle, 500 μM sodium (meta)arsenite (S7400, Sigma-Aldrich), or 50 μM 15d-PGJ2 (538927, EMD Millipore) in Opti-MEM. ASO electroporation was performed using the NEON Transfection System 10 μl-size kit (Thermo Fisher Scientific) according to the manufacturer's instructions. Briefly, ∼200 000 cells per condition were electroporated in Resuspension Buffer R (Thermo Fisher Scientific) with a final concentration of 22.5 μM ASO using the following pulse parameters: 1005 V, 35 ms width, two pulses. Cells were plated into Opti-MEM containing either 0.1% DMSO or 50 μM 15d-PGJ2 and allowed to re-attach for 2 h prior to fixation and immunostaining.

Immunocytochemistry and confocal fluorescence microscopy

Immunocytochemistry was performed as previously described (26). Cells were fixed with 4% formaldehyde in 1× PBS for 30 min at room temperature, permeabilized for 5 min with 0.1% Triton X-100, washed three times with 1× PBS, and blocked for 30 min at room temperature with 1 mg/ml BSA in 1× PBS. Primary antibody incubations were performed in blocking buffer (2 h at room temperature or overnight at 4°C) followed by three washes with 0.1% Nonidet P 40 substitute (74385, Sigma-Aldrich) in 1× PBS. Secondary antibody incubations were performed in blocking buffer (1 h at room temperature) followed by three washes with 0.1% Nonidet P 40 substitute in 1× PBS. Coverslips were mounted in ProLong Gold Antifade with DAPI (Thermo Fisher Scientific). All images were acquired on an Olympus FV1000 confocal microscope using a PlanApo N 60× O objective (N.A. = 1.42) with excitation at 405, 488, 543 and 635 nm. Image analysis was performed using Olympus Fluoview Ver2.1 or ImageJ-Fiji (50). For live cell imaging, cells were grown on 35-mm imaging dishes (MatTek), loaded with 1 μg/ml Hoechst 33342 (Thermo Fisher Scientific), and imaged in FluoroBrite DMEM (Thermo Fisher Scientific) using a Weather Station environmental chamber (Precision Control LLC) at 37°C. ASO signals may be observed outside the cellular boundaries due to the attachment of ASOs to the collagen-coated glass bottom dish.

Fluorescence *in situ* hybridization (FISH) detection of *NEAT1* lncRNA

A hybridization probe for detection of both *NEAT1*–1 and *NEAT1*–2 lncRNAs was prepared from HeLa genomic DNA (gDNA) isolated using the PureLink Genomic DNA isolation kit (Thermo Fisher Scientific). PCR was performed on gDNA with Phusion polymerase (New England Biolabs) and the following primers: h*NEAT1*-Forward 5′-GGTGTAGTTGTGGGGGAGGAAGTG-3′ and h*NEAT1*-Reverse-T7-promoter 5′- TAATACGACTCACTATAGGGGGCATGGACAAGTTGAAGATTAGCCC -3′ (underline indicates the T7 polymerase promoter). AlexaFluor-594-labeled probe was synthesized from the gel-purified PCR product using the FISH Tag Multicolor Kit (Thermo Fisher Scientific) according to the manufacturer's instructions. The probe was prepared less than 2 days before use and stored at –80°C. Cells were transiently transfected with tGFP-FUS-WT or tGFP-FUS-P525L plasmids for 24 h as described above, and subsequent processing steps were carried out using RNase-free reagents supplemented with RNaseOUT (Thermo Fisher Scientific). Following transfection, cells were fixed with 4% formaldehyde in 1× PBS for 30 min at room temperature, washed twice with 1× PBS, permeabilized with 0.4% Triton X-100 in 1× PBS for 5 min, washed three times with 1× PBS, and washed once in 2× SSC for 5 min. Probe hybridization mixture (50% formamide, 2× SSC, 5% dextran sulfate, 5 mM EDTA, 1× Denhardt's solution, 50 μg *Escherichia coli* tRNAs (Sigma-Aldrich), and 250 ng of labeled RNA probe) was heated for 10 min at 75°C and chilled immediately on ice. Hybridization was conducted in a dark humidified chamber at 55°C for 16 h. Cells were subsequently washed once with 0.1× SSC in 50% formamide for 20 min at 55°C and a second time for 20 min at room temperature before mounting in ProLong Gold Antifade with DAPI.

Fluorescence *in situ* hybridization (FISH) detection of poly(A) RNA

A hybridization probe consisting of 5′-Cy5-labeled $(dT)_{30}$ (Integrated DNA Technologies) was used to visualize poly(A) RNA in a manner similar to previous reports (43,51). Cells were transfected with plasmid for 18 h and cEt PS-ASO for an additional 6 h. All FISH buffers were supplemented with RNaseOUT. Cells were fixed with 4% formaldehyde in 1× PBS for 30 min at room temperature, washed twice with 1× PBS, permeabilized with 0.1% Triton X-100 in 1× PBS for 5 min, and washed once with 10% formamide in 1× SSC for 10 min at 37°C. Hybridization mixture (10% formamide, 10% dextran sulfate, 0.1 μM Cy5-labeled $(dT)_{30}$ and 1× SSC) was incubated with cells in a dark humidified chamber at 37°C for 2 h, followed by two washes with 10% formamide in 1× SSC for 10 min each at 37°C. Mounting and imaging were performed as described above.

Analysis of ASO colocalization with G3BP

All groups of images for comparative quantification were captured under identical non-saturating exposure settings, and colocalization analysis was performed using the JACoP plugin for ImageJ-Fiji (50,52). The thresholded Manders' colocalization coefficient method was chosen for all colocalization analyses because it does not require similar pixel intensities between channels (52) and thus provides an independent means of verifying the pixel intensity analyses based on regions of interest (ROI). Within a set of condi-

tions to be compared (e.g. DMSO, sodium arsenite and 15d-PGJ2), constant maximum and minimum threshold values were set and retained. To determine the amount of colocalization due to chance (inverted colocalization analysis), the G3BP channel in each image was rotated 180° and colocalization was measured again. For analyses of image fields, each field contained an average of approximately four cells.

ROI-based image analysis for granule/nuclear pixel intensity ratio

All groups of images for comparative quantification were captured under identical non-saturating exposure settings, and ROI-based image analysis was performed using ImageJ-Fiji macro scripts (50). For quantification of average pixel (px) intensity in the nucleus, the following operations were performed on each image: First, image bit depth in all slices was set to 8. To create a nuclear selection mask, a uniform absolute intensity threshold was applied to the DAPI channel and an ROI was created using the 'Analyze Particle' feature with a lower size limit of 5000 px^2. In the ASO channel to be measured, sliding paraboloid background subtraction (50 px radius) was performed, and the average pixel intensity in the ASO channel was measured within the DAPI-derived ROI. For quantification of average pixel intensity in tGFP, tGFP-FUS-P525L and tGFP-PSF-ΔNLS channels, the following operations were performed on each image: First, image bit depth in all slices was set to 8. To create a tGFP-derived (granule) selection mask, a uniform absolute intensity threshold was applied to the FITC channel and the 'Convert to Mask,' 'Create Selection' and 'Add to ROI Manager' features were used sequentially. In the ASO channel to be measured, sliding paraboloid background subtraction (50 px radius) was performed, and average pixel intensity inside the tGFP-derived ROI was determined.

Production of recombinant proteins and NanoBRET binding assays

The PURExpress *In Vitro* Protein Synthesis Kit (New England Biolabs), which is based on T7 polymerase and purified *E. coli* translational machinery, was used for coupled *in vitro* transcription and translation of proteins for binding assays. DNA constructs were cloned into the New England Biolabs DHFR Control Plasmid (hereafter called NEB-IVT) as detailed in Supplementary Table S1. *In vitro* transcription/translation reactions using these plasmid templates and supplemented with RNaseOUT were incubated for 2–4 h at 37°C with gentle agitation. After protein synthesis, reactions were diluted about 20-fold in Pierce IP lysis buffer (Thermo Fisher Scientific) on ice. Pierce anti-HA magnetic beads (88836, Thermo Fisher Scientific) or anti-FLAG magnetic beads (M8823, Sigma-Aldrich) for affinity tag purification were washed three times with IP lysis buffer and rocked with the diluted *in vitro* transcription/translation reactions for 1 h at 4°C. Magnetic beads were washed three times on ice with IP lysis buffer and resuspended in a fixed volume of IP lysis buffer. NanoBRET ASO binding assays were performed as previously described (31). First, the relative amount of purified protein per volume of magnetic bead suspension (based on nanoluciferase activity) was determined in 2× Binding Buffer (200 mM potassium acetate, 40 mM Tris pH 8.0, 2 mM EDTA, 0.02% NP-40, 6 μg/ml BSA and 1:1000 Promega Nano-Glo luciferase substrate) using an eight-point dilution curve over ∼3.5 orders of magnitude. In direct binding studies, AlexaFluor594-labeled ASOs were diluted in opaque-white 96-well plates using RNase-free water at concentrations spanning the pM to low μM range (50 μl/well final volume). In competitive binding experiments, a single concentration of AlexaFluor594-labeled ASO at approximately its K_D was mixed with varying concentrations of unlabeled ASOs spanning the pM to low μM range (50 μl/well final volume). Subsequently, 50 μl/well of 2× binding buffer containing 10^6 relative light units (RLU) of beads/well was added to the diluted ASOs, and plates were shaken for 10 min at room temperature. Nanoluciferase activity and BRET were measured in a Glowmax Discover plate reader as previously described (31). GraphPad Prism 6 was used to plot binding curves and calculate K_D values.

Arginine methylation of recombinant FUS *in vitro* using PRMT1

FUS-NLUC-FLAG was produced by *in vitro* transcription and translation using the PURExpress *In Vitro* Protein Synthesis Kit as described above. The *in vitro* translation reaction was subsequently diluted 1:10 in 1× HMT Reaction buffer supplemented with 200 μM *S*-adenosyl methionine (SAM) and 8 units of PRMT1 (New England Biolabs). In negative control reactions, water was substituted for SAM. Arginine methylation was performed for 1 h at 37°C. Methylation reactions were diluted 1:3 in Pierce IP buffer followed by anti-FLAG affinity purification and NanoBRET binding assays as described above.

SDS-PAGE and western blotting

Affinity purified recombinant proteins on magnetic beads were denatured at 95°C for 12 min in 1× NuPAGE LDS Sample Buffer (Thermo Fisher Scientific) supplemented 1:40 with β-mercaptoethanol. SDS-PAGE was performed with NuPAGE 4–12% Bis-Tris gradient gels in 1× MOPS buffer, and proteins were transferred to nitrocellulose membranes using an iBlot Dry Blotting System (Thermo Fisher Scientific). Membranes were blocked for 30 min at room temperature with 5% w/v nonfat dry milk in PBST (1× PBS with 0.1% Tween-20), except blots for anti-methyl arginine, which were blocked with 1% BSA in PBST. Blots were incubated with primary antibodies diluted in blocking buffer overnight at 4°C. Prior to secondary antibody incubation, membranes were washed three times for 10 min each with PBST at room temperature. HRP-conjugated secondary antibodies were incubated for 45 min at room temperature followed by three 10-min washes with PBST. Blots were developed using a Bio-Rad ChemiDoc XRS+ Molecular Imager and Amersham ECL Prime Western Blotting Detection Reagent (RPN2232, GE Healthcare Life Sciences).

Production of lentiviral particles and A431 stable line generation

DNA sequences encoding tGFP, tGFP-FUS-WT or tGFP-FUS-P525L were cloned into pLVX-IRES-Puro (Clontech) as described in Supplementary Table S1. Lenti-X 293T cells (Clontech) were seeded at 3–4 × 10^6 cells per 100-mm Matrigel-coated dish and co-transfected with 3 μg pLVX-IRES-Puro vector and 3 μg packaging plasmids using TurboFect. After 14 h, this medium was discarded, and cells were incubated with 5 ml of fresh medium for 12 h (10 ml total viral supernatant); the incubation with fresh medium was repeated. The supernatant was filtered through a 0.22-μm sterile syringe filter and stored at 4°C for no >5 days prior to use. A post-filtration viral titer of >5 × 10^5 infectious units/ml was confirmed using Lenti-X GoStix (Clontech). Viral transduction was performed on freshly attached (∼2 h after seeding) A431 cells in media containing 10 μg/ml polybrene (Santa Cruz Biotechnology). Viral supernatant was incubated with the cells at a multiplicity of infection of approximately 5 for 4–6 h, after which medium was replace with polybrene-containing media. At 48 h post-infection, A431 cells were passaged into media containing 0.5 μg/ml puromycin and grown for 7 days.

Statistical analysis

All statistical analyses were performed using IBM SPSS Statistics v20. Homogeneity of variance was assessed using Levine's test. For all analyses, $\alpha = 0.05$.

RESULTS

cEt PS-ASOs localize to cytoplasmic stress granules

Our recent work indicates that many intracellular ASO-binding proteins are nucleic acid binding proteins (25,28,29). In addition, many known PS-ASO binding proteins (including DDX6, DHX30, YBX1, HSP90 and KHSRP) are also components of cytoplasmic stress granules (25,38,53). To investigate whether PS-ASOs localize to stress granules, we transfected HeLa cells with a 5′-Cy3-labeled cEt-modified 5–10–5 gapmer PS-ASO (ION-598987) and induced stress granule formation by treatment of cells with an eIF2α-dependent (sodium arsenite) or an eIF2α-independent (15d-PGJ2) stress granule inducer. Under these conditions, a fraction of cellular cEt PS-ASO localized to G3BP-positive stress granules (Figure 1A, arrows). Localization of cEt PS-ASO to stress granules was quantified as an increased thresholded Manders' colocalization coefficient of Cy3-labeled cEt PS-ASO with G3BP (Figure 1B). The stress granule localization of the cEt PS-ASO was confirmed in experiments with a 5–10-5 cEt ASO of different sequence (ION-950432) delivered by electroporation (Supplementary Figure S1). These data suggest that localization of cEt PS-ASOs to stress granules is independent of ASO sequence and delivery methods.

cEt PS-ASOs localize to cytoplasmic granules seeded by mutant isoforms of FUS and PSF

Hundreds of different proteins have been identified as stress granule components (38,53), and the protein composition of stress granules can vary depending on the type of stress (54). These properties complicate the task of identifying individual proteins that might attract cEt PS-ASO to endogenous stress granules. However, several PS-ASO binding proteins such as FUS and PSF, which are components of the stress granule proteome (25,31,53), were previously shown to seed the formation of stress granule-like cytoplasmic aggregates when the nuclear import of these proteins is impaired (41,44,45,55–57). We therefore determined whether the formation of cytoplasmic FUS or PSF granules would alter PS-ASO localization. Consistent with previous reports (29,58), transiently expressed wild-type FUS fused to N-terminal turbo GFP (tGFP-FUS-WT) colocalized with cEt PS-ASO in the nucleoplasm and at nuclear paraspeckles (Figure 2A and B). However, expression of tGFP-FUS containing the ALS-linked P525L mutation (tGFP-FUS-P525L, Figure 2A), which disrupts the nuclear translocation of FUS (45,46), resulted in profound enrichment of cEt PS-ASO in G3BP-positive cytoplasmic FUS granules (Figure 2B, arrows). This phenotype was not unique to HeLa cells, as localization of cEt PS-ASO to cytoplasmic FUS-P525L granules containing G3BP was also observed in A431 cells stably expressing tGFP-FUS-P525L (Supplementary Figure S2). Substitution of the hemagglutinin (HA) tag for tGFP gave similar results with respect to FUS granule formation and cEt PS-ASO recruitment (Supplementary Figure S3).

Stress granules and FUS granules contain poly(A) RNA (43,59). Fluorescence *in situ* hybridization (FISH) using an oligo(dT) probe revealed that cEt PS-ASO and poly(A) RNA can simultaneously localize to FUS-P525L aggregates (Figure 2C, arrows, and Supplementary Figure S4). FUS is also required for the formation of paraspeckles and is known to associate with and regulate the level of the *NEAT1* RNA upon which paraspeckles are assembled (33,35,43,60). RNA-FISH revealed that both wild-type FUS and a residual pool of FUS-P525L within the nucleus can colocalize with *NEAT1* in nuclear paraspeckles, and *NEAT1* RNA did not re-localize to cytoplasmic FUS aggregates in cells overexpressing FUS-P525L (Supplementary Figure S5).

Given the ability of NLS-mutant FUS to recruit cEt PS-ASO to cytoplasmic aggregates, we asked if other paraspeckle proteins might exhibit similar behavior. PSF is another essential paraspeckle protein known to bind PS-ASOs with high affinity (25,29,31,61). PSF contains a classical NLS at the extreme C-terminus (amino acids 701–707, Figure 3A) (34,55). Expression of a PSF construct lacking this NLS resulted in cytoplasmic PSF aggregates that recapitulate the ability of FUS-P525L to attract cEt PS-ASO, G3BP, and poly(A) RNA (Figure 3B and C, arrows). Cells produced wild-type and NLS-mutant isoforms of FUS and PSF protein at roughly comparable levels, and ectopic expression of the mutants had little effect on the levels of endogenous FUS or PSF (Supplementary Figure S6).

To exclude the possibility that local sequestration of cEt PS-ASO is a non-specific property of all cytoplasmic protein aggregates, we also investigated TDP-43, an ALS-linked nucleic acid binding protein that is peripherally associated with paraspeckles (36,58,62). Wild-type TDP-43 fused to tGFP localized to the nucleoplasm and

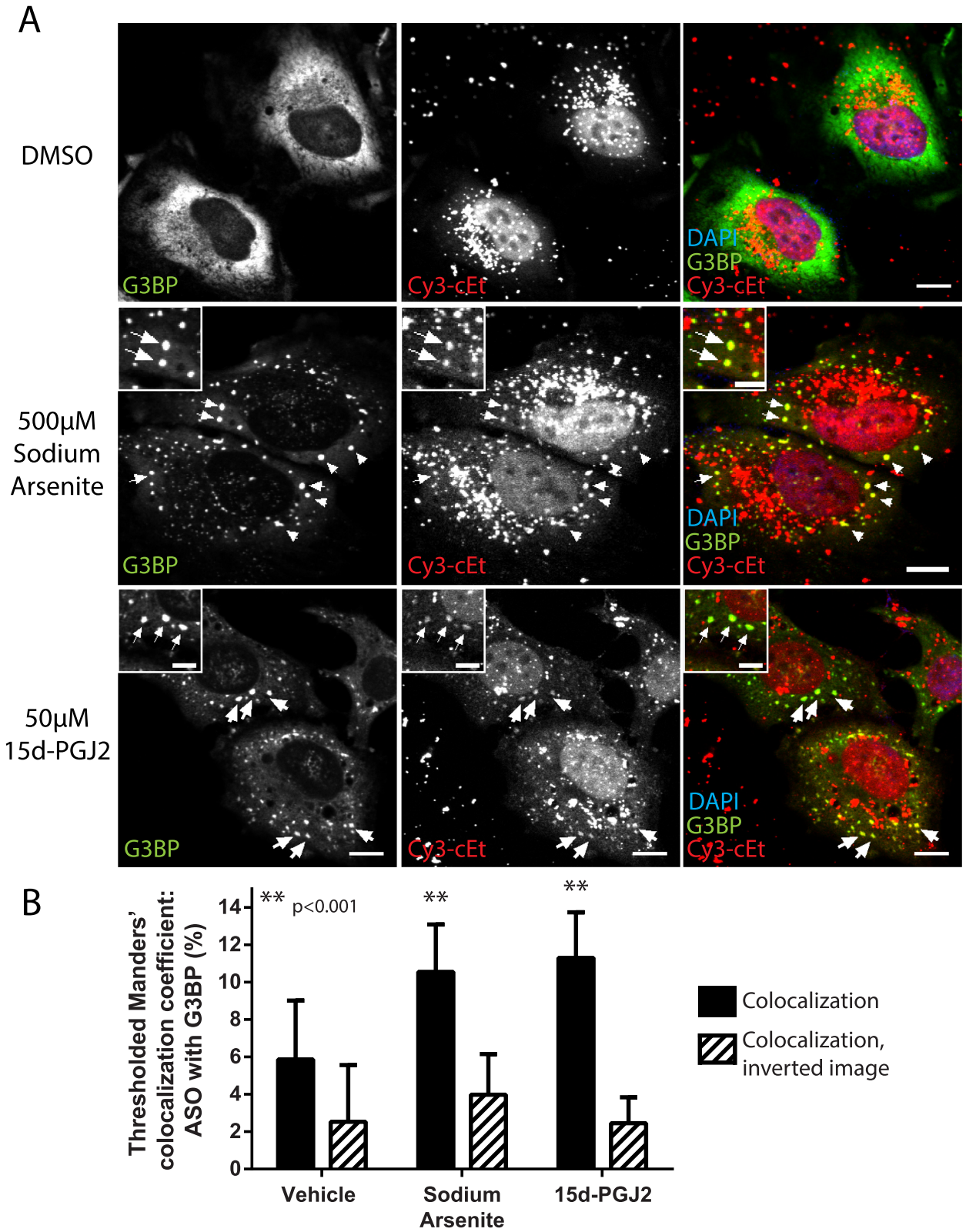

Figure 1. Cy3-labeled cEt PS-ASO localizes to stress granules formed by two different stress granule inducers. (**A**) Representative confocal immunofluorescence images of HeLa cells 5 h after lipid transfection with 50 nM Cy3-labeled cEt PS-ASO (ION-598987) under control conditions (0.1% DMSO) and after incubation of cells with eIF2α-dependent (sodium arsenite) or eIF2α-independent (15d-PGJ2) stress granule inducers for 1 h. Stress granules (cytoplasmic foci) positive for G3BP and cEt PS-ASO are indicated with arrows. Scale bars, 10 μm. Insert scale bars, 5 μm. (**B**) Colocalization between the Cy3-labeled cEt PS-ASO and G3BP was quantified by the thresholded Manders' colocalization coefficient method using the JACoP plugin for Fiji-ImageJ (** indicates $P < 0.001$ versus all other groups). Statistical analysis was performed using a univariate ANOVA with Tukey's HSD post hoc test ($n = 15$ image fields per group). Error bars represent ± S.D.

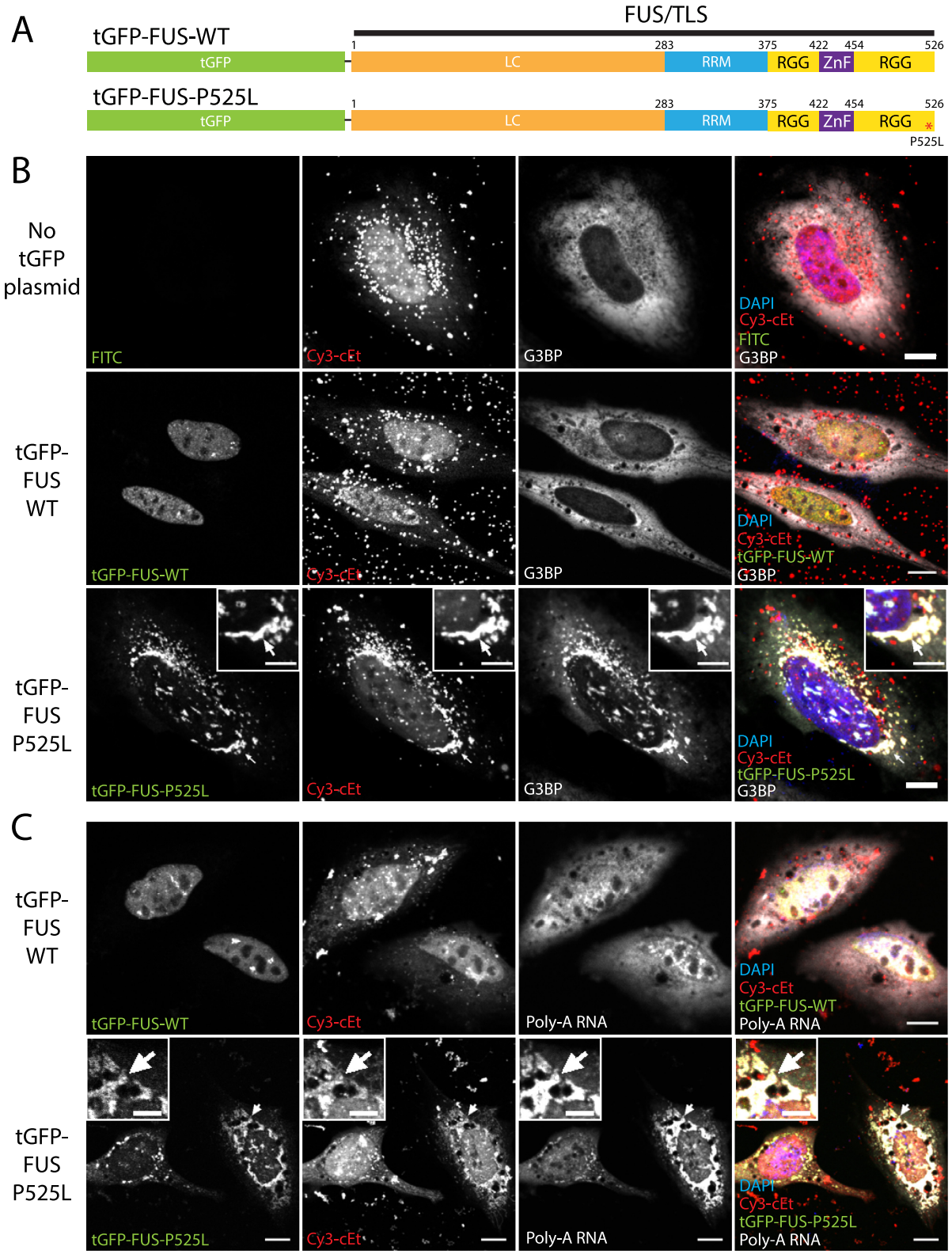

Figure 2. Expression of FUS-P525L stimulates the recruitment of cEt PS-ASO to G3BP and poly(A) RNA-positive cytoplasmic granules. (**A**) The domain structure of FUS includes a low-complexity domain (LC), an RNA-recognition motif (RRM), arginine-glycine-glycine repeats (RGG) and a zinc finger (ZF). Wild-type and P525L-mutant FUS were fused to N-terminal tGFP. (**B**) Representative confocal immunofluorescence images of HeLa cells revealed cEt PS-ASO (ION-598987) localization to the nucleoplasm and at nuclear paraspeckles in cells expressing wild-type FUS or without plasmid transfection. However, expression of tGFP-FUS-P525L recruited cEt PS-ASO to G3BP-positive cytoplasmic granules (arrows). (**C**) Cy5-oligo-dT(30) fluorescence *in situ* hybridization (FISH) revealed nuclear and cytoplasmic distribution of poly(A) RNA in wild-type FUS-expressing cells, whereas poly(A) RNA was colocalized with cEt PS-ASO (ION-598987) at cytoplasmic tGFP-FUS-P525L granules (arrows). Scale bars, 10 μm. Insert scale bars, 5 μm.

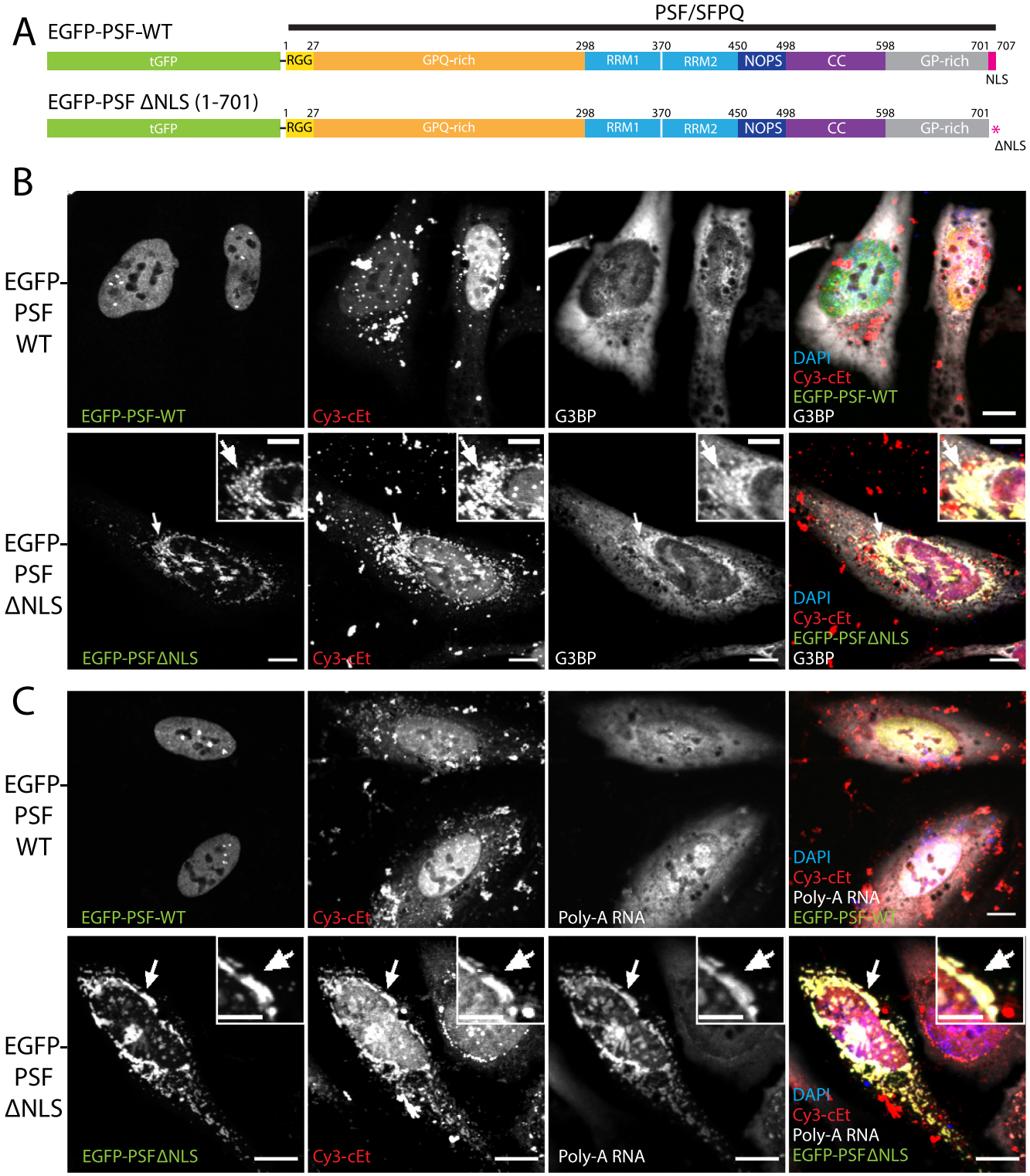

Figure 3. Expression of PSF-ΔNLS promotes recruitment of cEt PS-ASO to G3BP and poly(A) RNA positive cytoplasmic granules. (**A**) The domain structure of PSF includes: arginine–glycine–glycine repeats (RGG), a glycine–proline–glutamine rich domain (GPQ-rich), two RNA-recognition motifs (RRM1, RRM2), a NonA/paraspeckle domain (NOPS), a coiled-coil domain (CC), a glycine–proline rich domain (GP-rich), and a C-terminal nuclear localization sequence (amino acids 701–707, NLS). Wild type and ΔNLS-mutant PSF were fused to N-terminal tGFP. (**B**) Representative confocal immunofluorescence images of HeLa cells revealed cEt PS-ASO (ION-598987) localization to the nucleoplasm and at nuclear paraspeckles in cells expressing wild type PSF. However, expression of tGFP-PSF-ΔNLS recruited cEt PS-ASO to G3BP positive cytoplasmic granules (arrows). (**C**) Cy5-oligo-dT(30) fluorescence *in situ* hybridization (FISH) revealed nuclear and cytoplasmic distribution of poly(A) RNA in wild type PSF-expressing cells, whereas poly(A) RNA colocalized with cEt PS-ASO at cytoplasmic tGFP-PSF-ΔNLS granules (arrows). Scale bars, 10 μm. Insert scale bars, 5 μm.

to paraspeckles as expected (Supplementary Figure S7A). Whereas truncated TDP-43 lacking the N-terminal 89 amino acids (including the NLS, amino acids 78–89) mislocalized to the cytoplasm, we found that this truncated protein did not form aggregates and had no detectable effect on cEt PS-ASO localization (Supplementary Figure S7B). A previously characterized C-terminal TDP-43 fragment (amino acids 216–414) did formed cytoplasmic aggregates as previously reported (51,63,64), but these aggregates did not recruit cEt PS-ASO or G3BP (Supplementary Figure S7C–E). These observations suggest that cytoplasmic protein aggregates of a specific composition attract cEt PS-ASO.

Quantification of the cEt PS-ASO distribution between the nucleus and cytoplasmic granules

PS-ASOs are enriched in the nucleus under transfection or electroporation conditions (Figure 1A, Supplementary Figure S1A) (25,26,29). Therefore, we sought a method by which to semi-quantitatively compare the signal intensity of cEt PS-ASO in cytoplasmic granules with that in the nucleus under different experimental conditions. The thresholded Manders' colocalization coefficient method indicated an increase in colocalization of cEt PS-ASO with G3BP in cells that express FUS-P525L or PSF-ΔNLS (Figure 4A and B). This was true for two cEt PS-ASOs of different sequences with different fluorophore conjugates (ION-950431 and ION-766635). These results confirm our qualitative observations of cEt PS-ASO localization to G3BP-positive granules during FUS-P525L and PSF-ΔNLS expression.

Traditional colocalization analyses compare only two channels at a time, and a large number of two-channel colocalization comparisons (including inverted image negative controls) would be needed to adequately describe both nuclear and granule cEt PS-ASO localization within a four channel image. To address this issue, we developed a set of image quantification protocols using Fiji-ImageJ to estimate the amount of fluorescently labeled cEt PS-ASO in cytoplasmic granules and in the nucleus within individual cells (Figure 4C). Briefly, after confocal image acquisition under identical non-saturating exposure conditions, DAPI or tGFP channels were processed to automatically generate 'nuclear' and 'granule' selection masks. The average pixel intensity of cEt PS-ASO signal within these regions were then determined (Figure 4C). Results of this analysis based on regions of interest (ROI) indicated that cells expressing FUS-P525L or PSF-ΔNLS exhibited a median cEt PS-ASO granule/nucleus pixel intensity ratio between 2 and 3, whereas cells expressing tGFP alone yielded a median granule/nucleus intensity ratio ≤ 1 (Figure 4D and E). Expression of wild-type FUS or PSF resulted in a cEt PS-ASO granule/nuclear pixel intensity ratio of approximately 1, since tGFP-tagged wild-type FUS and PSF predominantly localize to the nucleoplasm (Figures 2B and 3B). These findings confirmed our qualitative imaging results and validated the ROI-based image quantification method as a rapid means of assessing ASO enrichment within subcellular regions bounded by signal from specific markers. Since cytoplasmic PSF-ΔNLS and FUS-P525L granules exhibit a similar degree of cEt PS-ASO recruitment (Figure 4A, B, D and E), subsequent experiments were performed using FUS-P525L and were quantified with the ROI-based method.

cEt PS-ASO is recruited to cytoplasmic FUS-P525L granules from an intracellular source

Since cytoplasmic FUS-P525L granules were unable to sequester *NEAT1* RNA from within the nucleus (Supplementary Figure S5), it is possible that cEt PS-ASO found at FUS-P525L granules might become trapped there after transfection but prior to nuclear entry. Alternatively, FUS-P525L granules might have the ability to redistribute cEt PS-ASO from other locations within the cell. To distinguish between these two possibilities, the order of the FUS plasmid expression and cEt PS-ASO transfection steps was reversed. Expression of FUS-P525L, but not wild-type FUS, before cEt PS-ASO transfection resulted in enrichment of cEt PS-ASO in cytoplasmic FUS granules (Figure 5A and B, arrows). Intriguingly, when cEt PS-ASO was pre-loaded into cells followed by washes and subsequent expression of the FUS plasmids over the period of 16 h, a similar degree of cEt PS-ASO recruitment to FUS-P525L granules was observed (Figure 5C and D, arrows). These findings confirm that cEt PS-ASO colocalized with FUS-P525L is indeed redistributed from an intracellular pool. Furthermore, these experiments were performed under live cell imaging conditions, indicating that cEt PS-ASO localization to FUS granules was not due to a fixation artifact.

2′ sugar modifications affect PS-ASO recruitment to cytoplasmic FUS-P525L granules

The number of PS backbone linkages as well type of 2′ sugar modification can substantially affect the protein binding profile of an ASO (25,28,29,32). We therefore examined the degree to which cytoplasmic FUS-P525L granules accumulate PS-ASOs of the same sequence but modified with MOE, cEt, or F. The median granule/nuclear intensity ratio was determined for each Cy3-labeled PS-ASO. An equal concentration (50 nM) of AlexaFluor647 (A647) labeled MOE PS-ASO was co-transfected with all Cy3-labeled PS-ASOs as a reference standard (1:1 ratio of Cy3-labeled PS-ASO and A647-labeled PS-ASO).

All PS-ASOs tested localized to FUS-P525L granules (Figure 6A–E, arrows). The cEt-modified PS-ASO had a granule/nuclear intensity ratio higher than ratios of the other PS-ASOs. The 2′- MOE, F and DNA PS-ASOs had more uniform distributions between the nucleus and cytoplasmic granules than did the cEt-modified PS-ASO (Figure 6A–E). In FUS-P525L expressing cells, the normalized nuclear intensity of Cy3-labeled cEt PS-ASO was slightly lower than those of the other PS-ASOs and the normalized nuclear intensity of Cy3-labeled DNA PS-ASO was slightly higher than those of the other PS-ASOs (Figure 6F); however, the total amount of granule and nuclear integrated signal density was similar across all Cy3-labeled PS-ASOs, indicating comparable overall transfection efficiency (Figure 6G).

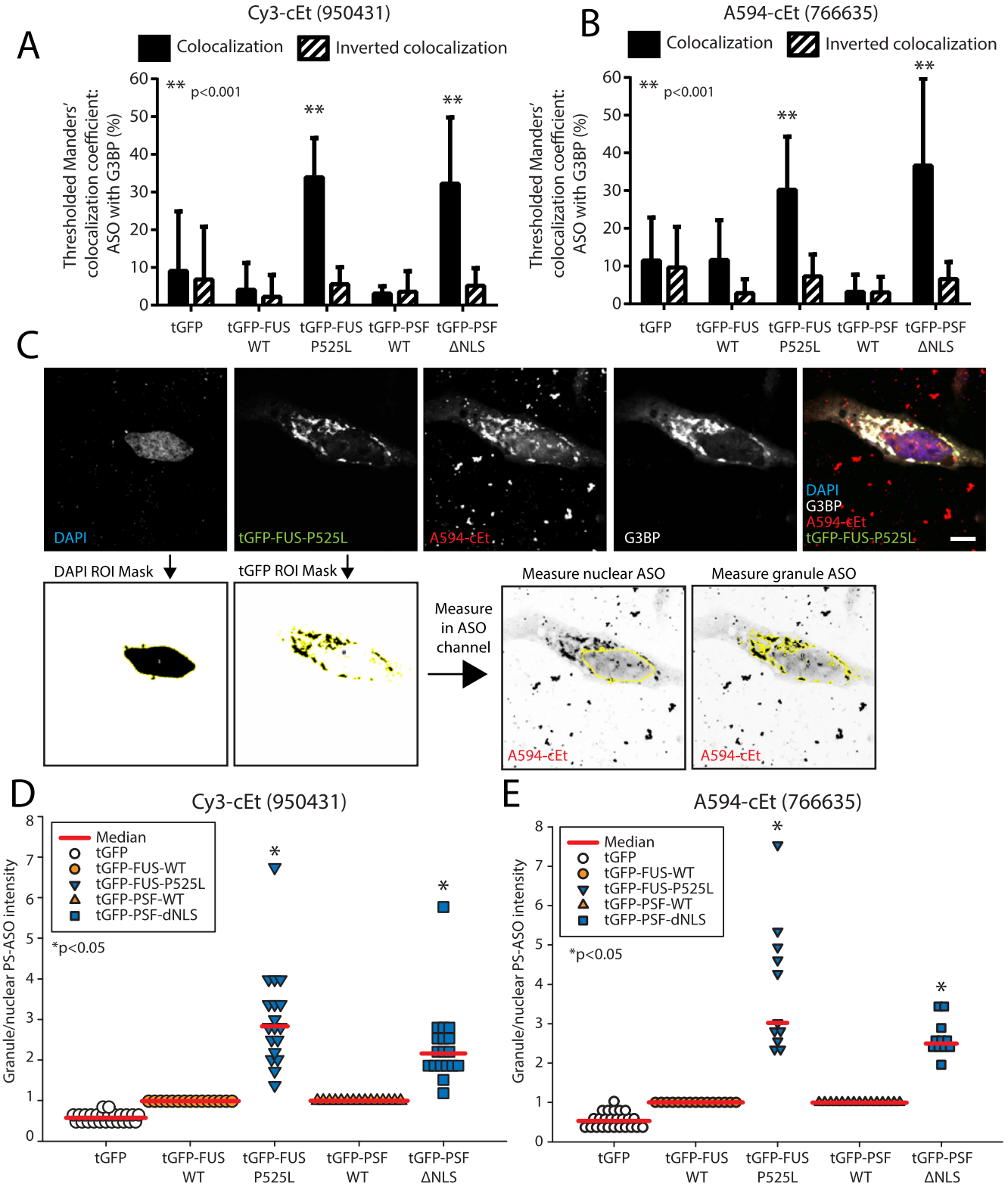

Figure 4. FUS-P525L and PSF-ΔNLS expression causes enrichment of cEt PS-ASOs with different sequences in cytoplasmic RNP granules. (**A**, **B**) HeLa cells transiently expressing tGFP-tagged wild type or NLS-mutant isoforms of FUS or PSF were subsequently transfected with fluorescently labeled cEt ASOs of different sequences (ION-950431 or ION-766635, 50 nM for 5 h). Images were analyzed using the thresholded Manders' colocalization coefficient method (** indicates $P < 0.001$ versus all other groups). Statistical analysis was performed using a univariate ANOVA with Tukey's HSD post hoc test ($n = 11$–25 cells per group), and error bars represent ± S.D. (**C**) An alternate method of semi-quantitative image analysis was performed on the same images using region of interest (ROI)-based selection and measurement. Scale bar, 10 μm. (**D**, **E**) The average granule/nuclear pixel intensity was measured for two cEt PS-ASOs with different fluorophore labels and sequences (ION-950431 and ION-766635) using the ROI-based quantification method. Each data point represents one cell ($n = 11$–25 cells per group), and statistical analysis was performed using the Kruskal–Wallis one-way analysis of variance (* indicates $P < 0.05$ versus wild type and tGFP groups).

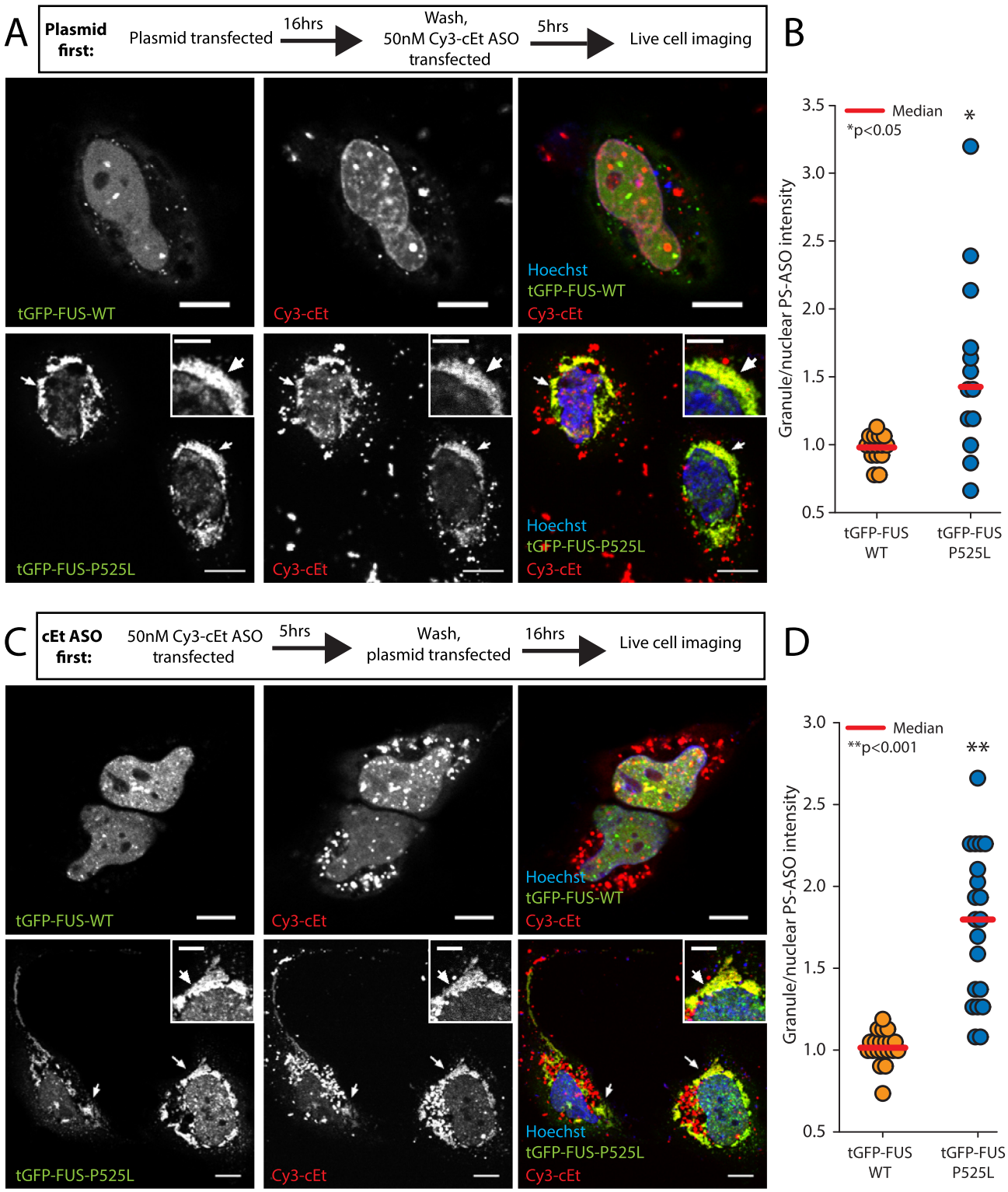

Figure 5. cEt PS-ASO is recruited to FUS-P525L granules from an intracellular source. (**A**) Representative confocal immunofluorescence images of live HeLa cells transiently expressing the tGFP-FUS-WT or tGFP-FUS-P525L plasmids prior to the transfection of a Cy3-labeled cEt PS-ASO (ION-598987, annotated as 'plasmid first'). (**B**) The average granule/nuclear pixel intensity was measured using ROI-based image quantification from the 'plasmid first' experimental design (n = 13–15 cells per group). (**C**) Representative confocal immunofluorescence images of live HeLa cells transfected first with Cy3-labeled cEt PS-ASO (ION-598987) followed by washes and subsequent expression of the tGFP-FUS-WT or tGFP-FUS-P525L plasmids (annotated as 'cEt ASO first'). (**D**) The average granule/nuclear pixel intensity was measured using ROI-based image quantification from the 'cEt ASO first' experimental design (n = 20 cells per group). Scale bars, 10 μm. Insert scale bars, 5 μm. Statistical analysis was performed using the Kruskal–Wallis one-way analysis of variance. In all images, arrows indicate tGFP-FUS-P525L granules.

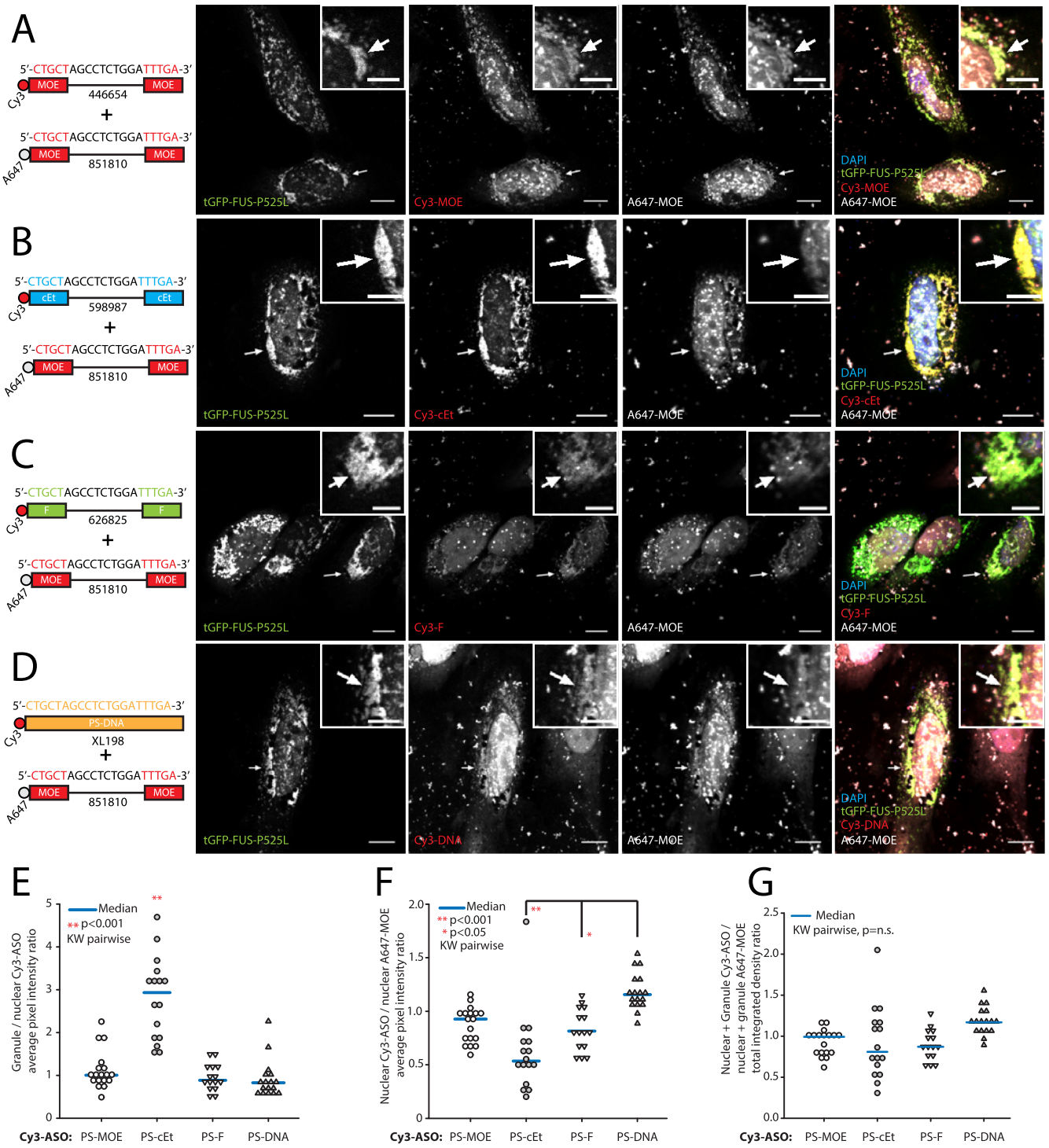

Figure 6. PS-ASO 2′ modifications influence ASO distribution between the nucleus and FUS-P525L granules. (**A**–**D**) HeLa cells transiently expressing tGFP-FUS-P525L were co-transfected for 5 h with equal amounts of an A647-labeled 2′ MOE PS-ASO (ION-851810) and a second Cy3-labeled PS-ASO of interest. All PS-ASOs consisted of the same sequence. Cy3-labeled PS-ASOs for each condition were: (A) MOE (ION-446654), (B) cEt (ION-598987), (C) 2′ F (ION-626825), (D) 2′ DNA (XL198). (**E**) ROI-based measurements of the average ASO pixel intensity in FUS-P525L granules compared to the nucleus. (F) A comparison of the average pixel intensity in the nucleus for Cy3 and A647 PS-ASOs. (**G**) The cellular loading of PS-ASOs into the granules and nucleus, calculated as the sum of total integrated Cy3 signal density in the nucleus + granule and normalized to the corresponding value for A647-MOE ASO in the same cell, did not significantly differ between the various Cy3-labeled PS-ASOs. In all images, arrows indicate tGFP-FUS-P525L granules. Scale bars, 10 μm. Insert scale bars, 5 μm. For dot density plots, each data point represents one cell and statistical analysis was performed using the Kruskal-Wallis one-way analysis of variance.

Despite the statistical homogeneity across these Cy3-labeled PS-ASO populations ($p>0.05$), it is evident that inclusion of the A647-labeled control PS-ASO did not completely correct for subtle variation in cell-to-cell transfection efficiency between the Cy3 and A647 PS-ASOs. Similarly, co-transfection of Cy3 and A647 labeled ASOs also had subtle (but not statistically significant) effects on the granule/nuclear distribution of the A647-labeled control PS-ASO (Supplementary Figure S8). Finally, qualitatively similar Cy3 ASO localization was observed in the absence of the A647 control PS-ASO (Supplementary Figures S9–S11). Cy3-labeled ASOs were localized to the nucleus in tGFP- or tGFP-FUS-expressing cells (Supplementary Figures S9 and S10, respectively), and Cy3-labeled cEt PS-ASO was robustly recruited to FUS-P525L aggregates (Supplementary Figure S11). Together, these results indicate that among commonly used sugar modifications, cEt PS-ASOs are more susceptible to sequestration at cytoplasmic FUS-P525L granules than are PS-DNA or PS-ASOs modified with MOE or F.

LNA-modified PS-ASOs robustly localize to endogenous stress granules and FUS-P525L granules

Upon finding that cEt-modified PS-ASOs were more dramatically enriched at FUS-P525L granules than were PS-DNA or PS-ASOs modified with MOE or F, we wondered if this behavior might extend to PS-ASOs containing other 2′,4’ constrained nucleotides such as locked nucleic acids (LNAs). A FITC-labeled LNA PS-ASO (ION-391857) robustly localized to endogenous stress granules under conditions of lipid transfection (Supplementary Figure S12) and electroporation (Supplementary Figure S13). Additionally, the FITC-labeled LNA PS-ASO was enriched at HA-FUS-P525L granules with a granule/nuclear intensity ratio of between 1.5 and 2, which was comparable to that of Cy3-labeled cEt PS-ASOs (Supplementary Figure S14). Based on these results, it appears that PS-ASOs containing 2′4’ constrained nucleic acids more generally exhibit enhanced localization to cytoplasmic RNP granules.

Characterization of the domain requirements for FUS-PS-ASO binding using *in vitro* NanoBRET

Based on the relatively high affinity ($K_D < 20$ nM) of FUS for PS-ASOs (31), it is possible that the localization of PS-ASO to cytoplasmic FUS granules reflects direct ASO–protein binding. Although several studies have investigated the *in vitro* binding properties of FUS domains to a variety of endogenous nucleic acids (65–67), the effects of a PS backbone and 2′ modifications on nucleic acid binding to FUS have not been thoroughly examined. Although PS and 2′ modifications have long been known to affect protein binding (17,68), the contribution of different types of nucleic acid binding protein domains to PS-ASO interactions has only been explored in detail for a few proteins (28,31). Here we utilized a recently described bioluminescence resonance energy transfer (BRET) assay (31) based on nanoluciferase (NLUC), a 19-kDa luciferase variant that produces much brighter and more sustained luminescence than *Renilla* luciferase (69). In our implementation of the NanoBRET assay, a NLUC-tagged protein of interest was produced using *in vitro* transcription and translation system, affinity purified using an epitope tag, and bound to an AlexaFluor594 (A594)-labeled ASO, which served as the BRET acceptor. The amplitude of the BRET ratio (acceptor emission to donor emission) can also provide information about the physical proximity of the ASO binding site relative to NLUC (31,69).

Four FUS-P525L protein truncations (termed FUS-N, -NR, -RRM and -Z) and two full-length FUS-P525L constructs (with N- or C-terminal NLUC fusions) were designed based on previous work (65,66) (Figure 7A). Following expression and affinity purification, correctly sized protein products were verified by western blot (Figure 7B). NanoBRET binding assays were conducted using 10^6 RLU of each protein and A594-labeled MOE, cEt and F PS-ASO (ION-766633, ION-766635 and ION-766637, respectively) concentrations spanning the pM to low μM range. The PS-ASO sequence used does not contain a consensus FUS binding sequence (70), and, since *in vitro* binding of FUS is reported to be relatively promiscuous with regard to sequence (65), we chose to examine the effects of various backbone and 2′-modifications for this single sequence.

In agreement with a previous report (31), the 2′-F PS-ASO bound to full-length FUS with 5–10-fold higher affinity than MOE or cEt PS-ASOs (Figure 7C–E, 2′-F PS-ASO $K_D = 2.2 \pm 0.2$ nM). Interestingly, whereas the K_D measured for full-length FUS-P525L was not significantly different using N- or C-terminally fused NLUC, C-terminal NLUC gave a significantly higher amplitude BRET ratio (Figure 7C–E), suggesting that at least one PS-ASO binding site is near the C-terminus. Consistent with this finding and with previous literature (65,66), the second largest BRET ratio was produced by the FUS-Z truncation, which includes the C-terminal RGG-ZF-RGG domains and is known to bind nucleic acids (Figure 7C–E, (65)). The FUS-NR truncation containing the low complexity (LC) and RRM domains exhibited high affinity binding and a high amplitude BRET ratio, although the LC and the RRM domains in isolation did not bind PS-ASOs as efficiently (Figure 7C–E). This suggests that PS-ASOs also bind to a second site formed by the combination of the LC and RRM domains. NLUC-HA alone bound poorly to PS-ASOs within the concentration range of the assay (Figure 7C–E).

FUS-Z domain RGG repeats contribute to the interaction with ASOs

We next investigated the contribution of the FUS-Z domains to ASO binding using additional constructs. In the context of full-length FLAG-tagged FUS-P525L, we either removed the RanBP2-type zinc finger (ZF) or mutated all C-terminal arginines between amino acids 375 and 526 to serine (excluding those within the ZF domain, Figure 8A and B). A similar RGG to SGG mutation strategy was recently shown to prevent recruitment of FUS to sites of DNA damage by negatively charged poly(ADP-ribose) (71). NanoBRET binding studies revealed that deletion of the ZF did not significantly affect BRET amplitude or affinity. The R/S mutations within the RGG domains dramati-

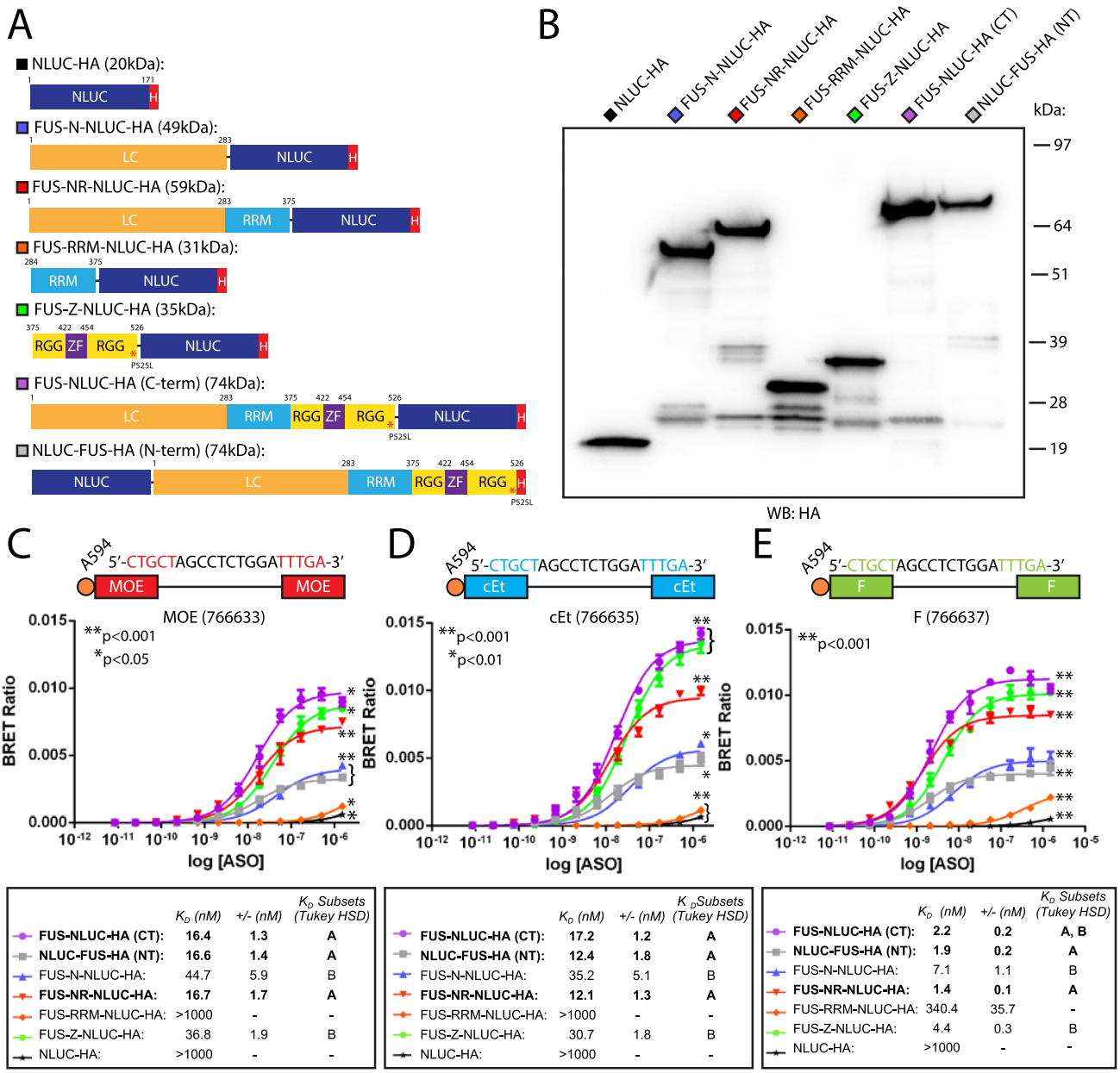

	K_D (nM)	+/- (nM)	K_D Subsets (Tukey HSD)
FUS-NLUC-HA (CT):	**16.4**	**1.3**	**A**
NLUC-FUS-HA (NT):	**16.6**	**1.4**	**A**
FUS-N-NLUC-HA:	44.7	5.9	B
FUS-NR-NLUC-HA:	**16.7**	**1.7**	**A**
FUS-RRM-NLUC-HA:	>1000	-	-
FUS-Z-NLUC-HA:	36.8	1.9	B
NLUC-HA:	>1000	-	-

	K_D (nM)	+/- (nM)	K_D Subsets (Tukey HSD)
FUS-NLUC-HA (CT):	**17.2**	**1.2**	**A**
NLUC-FUS-HA (NT):	**12.4**	**1.8**	**A**
FUS-N-NLUC-HA:	35.2	5.1	B
FUS-NR-NLUC-HA:	**12.1**	**1.3**	**A**
FUS-RRM-NLUC-HA:	>1000	-	-
FUS-Z-NLUC-HA:	30.7	1.8	B
NLUC-HA:	>1000	-	-

	K_D (nM)	+/- (nM)	K_D Subsets (Tukey HSD)
FUS-NLUC-HA (CT):	**2.2**	**0.2**	**A, B**
NLUC-FUS-HA (NT):	**1.9**	**0.2**	**A**
FUS-N-NLUC-HA:	7.1	1.1	B
FUS-NR-NLUC-HA:	**1.4**	**0.1**	**A**
FUS-RRM-NLUC-HA:	340.4	35.7	-
FUS-Z-NLUC-HA:	4.4	0.3	B
NLUC-HA:	>1000	-	-

Figure 7. Multiple domains within FUS bind MOE-, cEt- and F-modified PS-ASOs *in vitro*. (**A**) For NanoBRET binding assays, Nanoluciferase was fused to different domains of FUS as well as to the N- or C-terminus of full length FUS-P525L. (**B**) Western blot analysis confirmed the expression of the recombinant proteins. Approximate molecular masses are noted at the right in kDa. (**C**–**E**) NanoBRET binding assays were performed using 10^6 RLU of each protein and 5′-A594-labeled (C) MOE (ION-766633), (D) cEt (ION-766635) and (E) 2′ F (ION-766637) ASOs in concentrations from ∼10 pM to 1 μM. All PS-ASOs were composed of the same sequence. Statistical analysis on maximum binding curve amplitudes (B_{max}) was performed using the univariate ANOVA with Tukey's HSD post hoc (* and ** on the graphs indicate $P < 0.05$ and $P < 0.001$, respectively, versus all other groups). Curved brackets indicate no significant difference in Bmax between the bracket-enclosed groups. Binding experiments were performed in triplicate and error bars represent ± S.D. Relative K_D values are presented as average ± S.D. Statistical analysis on the binding curve affinities (K_D) was performed using the univariate ANOVA with Tukey's HSD post hoc (bold text as well as the 'K_D subsets' column indicates statistically homogenous groups among which there is no significant difference in K_D). Groups marked with a dash (–) were not included in statistical analysis of the K_D because they exhibited a poor fit to the standard sigmoidal binding curve ($R^2 < 0.7$).

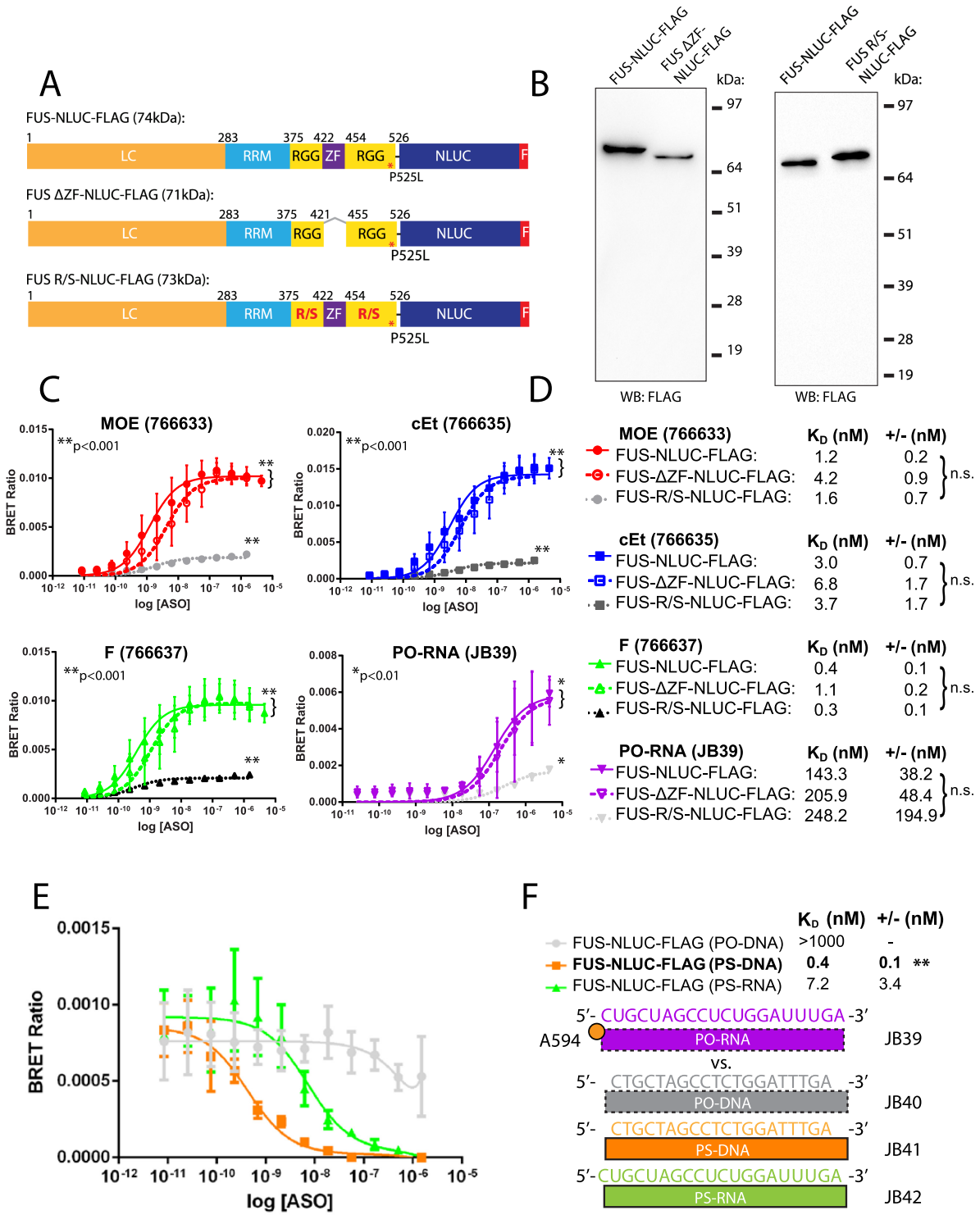

Figure 8. Characterization of the FUS RGG and zinc finger domains in binding to ASOs with different 2′ modifications and backbone chemistries. (**A**) Nanoluciferase (NLUC) and a FLAG affinity tag were fused to the C-termini of full-length FUS-P525L (FUS-NLUC-FLAG), FUS-P525L lacking the zinc finger (FUS ΔZF-NLUC-FLAG) and FUS-P525L in which all arginines within the FUS Z domain (excluding those in the zinc finger) were mutated to serine (FUS R/S-NLUC-FLAG). (**B**) Western blot analysis confirmed the expression of the recombinant proteins. Approximate molecular masses are noted at the right in kDa. (**C**, **D**) NanoBRET binding assays were performed using the following ASOs: MOE: ION-766633, cEt: ION-766635, F: ION-766637, PO-RNA: JB-39. K_D, n.s. indicates $P > 0.05$ by univariate ANOVA with Tukey's HSD post hoc. B_{max}, * and ** on the graphs indicate $P < 0.05$ and $P < 0.001$, respectively, vs. all other groups. Curved brackets indicate no significant difference in Bmax between the bracket-enclosed groups. (**E**, **F**) Competitive NanoBRET binding assays were performed against the A594-labeled PO-RNA ASO (JB-39) at approximately its K_D. Unlabeled PO-DNA, PS-DNA or PS-RNA ASOs of the same sequence were added at concentrations between ∼10 pM and 5 μM. Binding experiments were performed $n =$ 3–6 times per group and error bars represent ± S.D. Relative K_D values are presented as average ± S.D. Statistical analysis on the binding curve affinities (K_D) and amplitudes (B_{max}) was performed using the univariate ANOVA with Tukey's HSD post hoc.

cally reduced the BRET amplitude but did not significantly change affinity relative to the full-length FUS-P525L (Figure 8C and D). These results are consistent with the protein containing a higher affinity ASO binding site formed by the LC and RRM domains and a lower affinity site at the C-terminus that is presumably mediated by interactions between arginines and the nucleic acid backbone (72,73). Although the absolute K_D values obtained using proteins purified on anti-FLAG beads were uniformly lower than those measured on anti-HA beads in Figure 7, a similar rank order of binding (F > cEt/MOE) was observed (Figure 8D).

To better understand how ASO modifications contribute to ASO-FUS binding, we compared the binding of PS-ASOs to a PO-RNA of the same sequence (JB-39). The A594-labeled PO-RNA bound to FUS-P525L with 100- to 300-fold lower affinity than PS-ASOs (PO-RNA K_D = 143.3 ± 38.2 nM), although the magnitudes of changes in BRET amplitude and binding affinity produced by ZF deletion and R/S mutations were similar to those observed for PS-ASOs (Figure 8C and D). Competition binding was performed between this A594-labeled PO-RNA and unlabeled PO-DNA, PS-DNA, or PS-RNA of the same sequence (JB-40, JB-41 and JB-42, respectively). Results indicated that although the PS moiety greatly contributes to high affinity ASO-FUS binding, DNA bound with considerably higher affinity than RNA in the context of a PS backbone (Figure 8E and F).

An N-terminal region adjacent to the FUS RRM domain enhances its binding affinity for PS-ASOs

Based on the NanoBRET binding experiments, the highest affinity PS-ASO binding site on FUS appeared to require the both LC and RRM domains, since neither domain alone was sufficient for high affinity PS-ASO binding. To further characterize this N-terminal binding site constructs FUS-R1-NLUC-HA and FUS-R2-NLUC-HA were prepared that have additional upstream protein sequence compared to FUS-RRM (Figure 9A and B). FUS-R1, which is 70 amino acids longer than FUS-RRM, exhibited binding that was not significantly different in BRET amplitude or affinity from FUS-NR (Figure 9C–E). The FUS-R2 construct, which is 41 amino acids longer than FUS-RRM, had reduced binding affinity and slightly reduced BRET amplitude to the cEt PS-ASO compared to FUS-NR (Figure 9C–E). These results indicated that the FUS-R1 construct (FUS amino acids 213–375) encompasses a high affinity PS-ASO binding site.

Arginines within the C-terminal RGG domain of FUS mediate FUS-Z binding to PS-ASO

We next analyzed the C-terminal motifs within FUS-Z. The two RGG repeat-containing domains of FUS flank a central zinc finger. The zinc finger itself appeared to be largely dispensable for PS-ASO interactions, whereas the RGG domains were not (Figure 8C and D). Therefore, we chose to investigate the PS-ASO binding ability of each RGG domain within FUS-Z separately using four additional NLUC fusion constructs. Two of these constructs were either the N-terminal or C-terminal RGG domain alone, and two consisted of FUS-Z with arginine to serine mutations throughout either the N- or C-terminal RGG domain (Figure 10A and B). NanoBRET binding assays performed on the *in vitro* translated and purified proteins indicated that constructs containing an intact extreme C-terminal RGG domain (CT-RGG-NLUC-HA and NT-R/S-NLUC-HA) largely recapitulated the PS-ASO binding profile of the intact FUS-Z region. Inclusion of the zinc finger (NT-R/S-NLUC-HA) increased in affinity for the 2′-F PS-ASO but not for the other PS-ASOs (Figure 10C–E). In contrast, the N-terminal RGG domains (NT-RGG-NLUC-HA and CT-R/S-NLUC-HA) bound PS-ASOs with more than 5-fold lower affinity than did CT-RGG-NLUC-HA. The BRET amplitudes also decreased with the physical distance of the binding site from NLUC since the NT-RGG-NLUC-HA construct bound with higher amplitude than the CT-R/S-NLUC-HA construct (Figure 10C–E).

Arginine methylation by PRMT1 does not affect *in vitro* binding between FUS and PS-ASOs

Several prior studies have shown that methylation of arginines within the FUS C-terminus regulates transportin-mediated shuttling of FUS between the nucleus and cytoplasm (45,49,74,75). Since C-terminal arginines also contribute to the PS-ASO binding affinity of FUS (Figures 8 and 10), we investigated the impact of arginine methylation of recombinant FUS-NLUC-FLAG by the methyltransferase PRMT1 on PS-ASO binding. FUS-NLUC-FLAG was produced by *in vitro* transcription/translation and was incubated in solution with PRMT1 in the presence or absence of the essential methyl donor *S*-adenosyl methionine (SAM) prior to anti-FLAG affinity purification. Western blotting for mono- and dimethyl arginine indicated substantial methylation of FUS-NLUC-FLAG that was SAM-dependent (Supplementary Figure S15A). No significant differences in PS-ASO binding were observed between methylated and unmethylated FUS-NLUC-FLAG (Supplementary Figure S15B), indicating that methylation of FUS does not alter its PS-ASO binding ability *in vitro*.

Cytoplasmic aggregates of β23-FUS-Z are sufficient to recruit cEt PS-ASO in cells

Given that the FUS-Z domain alone is sufficient to bind cEt PS-ASO *in vitro* with reasonably high affinity, we asked whether this domain of FUS could mediate cEt PS-ASO recruitment to artificial protein aggregates in the cytoplasm in HeLa cells. To address this question, we fused FUS-Z to a nuclear export signal (NES) and a computationally designed β-sheet-forming protein (β23) that is known to aggregate when expressed in cells (51,76). First, we confirmed that FUS-Z retained its ability to bind PS-ASOs *in vitro* when fused to HA-NES-β23 and that the corresponding R/S mutant of FUS-Z or β23 alone did not appreciably bind PS-ASOs (Supplementary Figure S16). In agreement with the *in vitro* binding data, when these constructs were expressed in HeLa cells as β23-tGFP fusion proteins, only the aggregates containing wild-type FUS-Z (β23-tGFP-FUS-Z) colocalized with cEt PS-ASO (Figure 11A–D, arrows). Although the fluorescent signal of the β23-

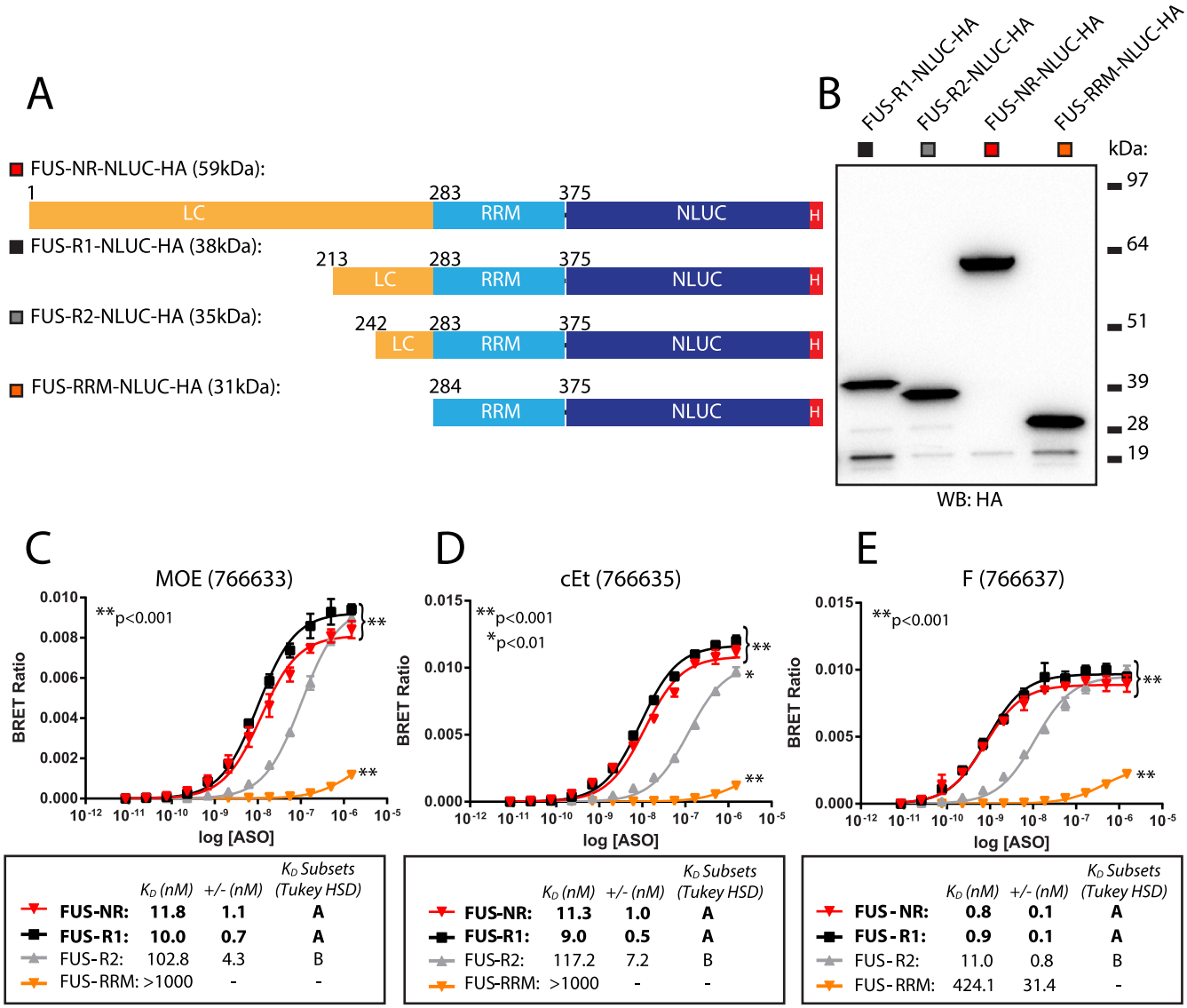

Figure 9. An N-terminal region adjacent to the FUS RRM domain enhances its binding affinity for PS-ASOs. (**A**) Two Nanoluciferase and HA tagged domain truncations, FUS-R1-NLUC-HA and FUS-R2-NLUC-HA, were constructed to contain ∼70 or ∼40 amino acids upstream of the FUS-RRM domain, respectively. (**B**) Western blot analysis confirmed the expression of the recombinant proteins. Approximate molecular masses are noted at the right in kDa. (**C**–**E**) NanoBRET binding assays for (C) 2′ MOE, (D) cEt, (E) and 2′ F PS-ASOs were performed. Statistical analysis on maximum binding curve amplitudes (B_{max}) was performed using the univariate ANOVA with Tukey's HSD post hoc (* and ** on the graphs indicate $P < 0.01$ and $P < 0.001$, respectively, versus all other groups). Curved brackets indicate no significant difference in B_{max} between the bracket-enclosed groups. Binding experiments were performed in triplicate and error bars represent ± S.D. Relative K_D values are presented as average ± S.D. Statistical analysis on the binding curve affinities (K_D) was performed using the univariate ANOVA with Tukey's HSD post hoc (bold text as well as the 'K_D subsets' column indicates statistically homogenous groups among which there is no significant difference in K_D). Groups marked with a dash (–) were not included in statistical analysis of the K_D because they exhibited a poor fit to the standard sigmoidal binding curve ($R^2 < 0.7$).

tGFP constructs was weak compared to that of tGFP-FUS-P525L (perhaps due to low expression, impaired translation, or protein misfolding), we verified that all β23-tGFP constructs were indeed expressed in HeLa cells (Figure 11E). Interestingly, G3BP localization did not appear to be greatly altered by the presence of any β23-tGFP aggregate (Figure 11A–C, arrows), suggesting that enrichment of cEt PS-ASO at β23-tGFP-FUS-Z aggregates may be a consequence of direct interaction with FUS-Z or FUS-Z interacting factors.

To further examine the specificity of cEt PS-ASO recruitment to different types of cytoplasmic granules, we performed an experiment in which cells expressing each β23-tGFP construct were stressed with sodium arsenite. In this way, the recruitment of PS-ASO to β23-tGFP aggregates and endogenous stress granules could be examined simultaneously within the same individual cells. Consistent with our previous findings, cells expressing β23-tGFP alone or mutant β23-tGFP-FUS-Z-R/S recruited cEt PS-ASO and G3BP to endogenous stress granules but not to the β23-tGFP aggregates (Supplementary Figure S17A-C,

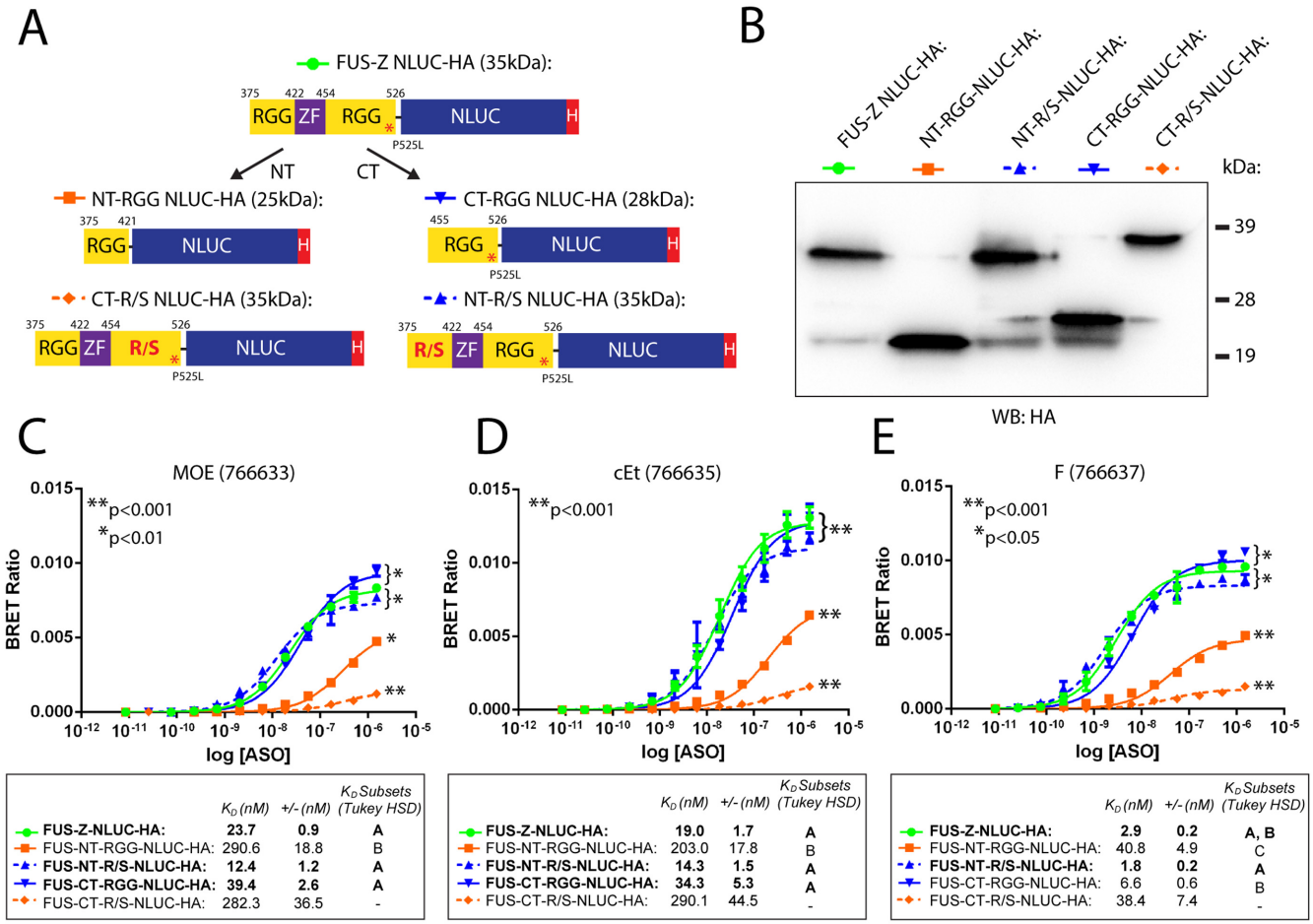

	K_D (nM)	+/- (nM)	K_D Subsets (Tukey HSD)
FUS-Z-NLUC-HA:	**23.7**	**0.9**	**A**
FUS-NT-RGG-NLUC-HA:	290.6	18.8	B
FUS-NT-R/S-NLUC-HA:	**12.4**	**1.2**	**A**
FUS-CT-RGG-NLUC-HA:	**39.4**	**2.6**	**A**
FUS-CT-R/S-NLUC-HA:	282.3	36.5	-

	K_D (nM)	+/- (nM)	K_D Subsets (Tukey HSD)
FUS-Z-NLUC-HA:	**19.0**	**1.7**	**A**
FUS-NT-RGG-NLUC-HA:	203.0	17.8	B
FUS-NT-R/S-NLUC-HA:	**14.3**	**1.5**	**A**
FUS-CT-RGG-NLUC-HA:	**34.3**	**5.3**	**A**
FUS-CT-R/S-NLUC-HA:	290.1	44.5	-

	K_D (nM)	+/- (nM)	K_D Subsets (Tukey HSD)
FUS-Z-NLUC-HA:	**2.9**	**0.2**	**A, B**
FUS-NT-RGG-NLUC-HA:	40.8	4.9	C
FUS-NT-R/S-NLUC-HA:	**1.8**	**0.2**	**A**
FUS-CT-RGG-NLUC-HA:	6.6	0.6	B
FUS-CT-R/S-NLUC-HA:	38.4	7.4	-

Figure 10. C-terminal arginines are largely responsible for the PS-ASO binding properties of the FUS-Z domain. (**A**) To measure the binding contribution of the FUS-Z domain N-terminal and C-terminal RGG wings separately, each wing (FUS NT-RGG and FUS CT-RGG) was fused to Nanoluciferase (NLUC) as well as an HA affinity tag. Two additional FUS-Z constructs containing arginine-to-serine mutations in the opposite RGG wing (FUS CT-R/S and FUS NT-R/S) were designed to account for potential effects of other motifs as well as physical proximity to nanoluciferase on the PS-ASO binding profile. (**B**) Western blot analysis confirmed the expression of the recombinant proteins. Approximate molecular masses are noted at the right in kDa. (**C**–**E**) NanoBRET binding assays for (C) 2′ MOE, (D) cEt, (E) and 2′ F PS-ASOs were performed. Statistical analysis on maximum binding curve amplitudes (Bmax) was performed using the univariate ANOVA with Tukey's HSD post hoc (* and ** on the graphs indicate $P < 0.05$ and $P < 0.001$, respectively, versus all other groups). Curved brackets indicate no significant difference in B_{max} between the bracket-enclosed groups. Binding experiments were performed in triplicate and error bars represent ± S.D. Relative K_D values are presented as average ± S.D. Statistical analysis on the binding curve affinities (K_D) was performed using the univariate ANOVA with Tukey's HSD post hoc (bold text as well as the 'K_D subsets' column indicates statistically homogenous groups among which there is no significant difference in K_D). Groups marked with a dash (–) were not included in statistical analysis of the K_D because they exhibited a poor fit to the standard sigmoidal binding curve ($R^2 < 0.7$).

solid arrows indicate endogenous stress granules while outlined arrows indicate β23-tGFP aggregates). In contrast, sodium arsenite-stressed cells expressing wild-type β23-tGFP-FUS-Z recruited cEt PS-ASO to both endogenous stress granules and β23-tGFP-FUS-Z aggregates (Supplementary Figure S17B, solid arrows). Interestingly, a fraction of the β23-tGFP-FUS-Z protein was itself recruited to G3BP-positive stress granules under these conditions, which was not observed for the other β23-tGFP fusion proteins (Supplementary Figure S17B, solid arrows). Image quantification indicated that enrichment of cEt PS-ASO at β23-tGFP-FUS-Z aggregates as well as colocalization between cEt PS-ASO and G3BP persisted after treatment with sodium arsenite (Supplementary Figure S17D and E). A similarly designed experiment using wild-type TDP43 and its C-terminal aggregation-prone fragment (amino acids 216–414) revealed that cEt PS-ASO was recruited to endogenous stress granules but not to TDP43 (216–414) aggregates (Supplementary Figure S18, solid arrows indicate endogenous stress granules while outlined arrows indicate TDP43-derived aggregates). These findings together support the conclusion that only cytoplasmic granules of a specific composition are able to attract significant amounts of cEt PS-ASO.

DISCUSSION

In this study, we report that PS-ASOs robustly localize to endogenous cytoplasmic stress granules as well as to cytoplasmic RNP granules seeded by the aggregation of NLS-mutant FUS or PSF. This phenotype is evident in both fixed and live cells of multiple types and appears to involve the re-

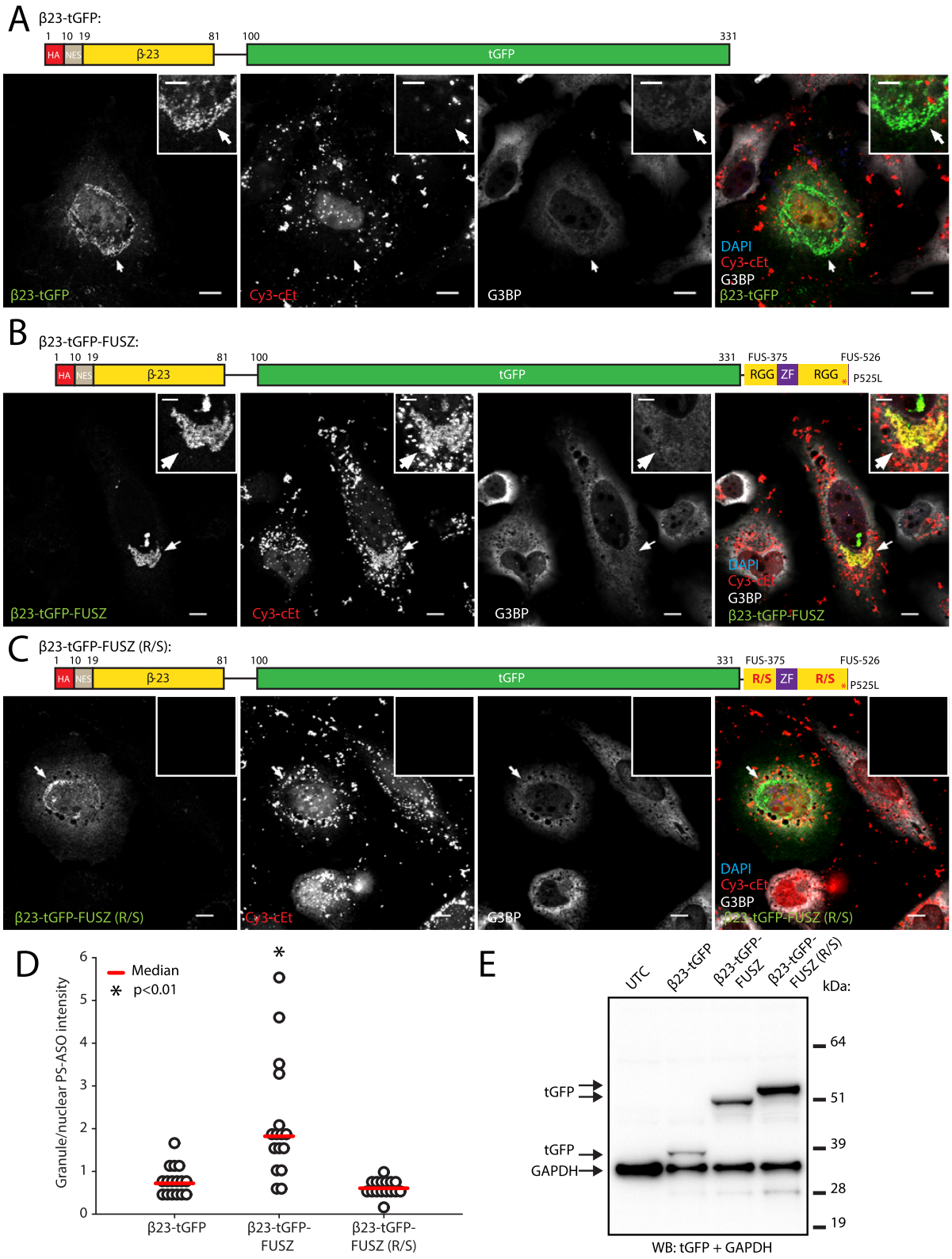

Figure 11. The FUS-Z domain is sufficient to recruit cEt PS-ASO to cytoplasmic aggregates formed by the artificial β-sheet protein β23 (**A**–**C**) Representative confocal immunofluorescence images of HeLa cells expressing (A) β23-tGFP, (B) β23-tGFP-FUSZ or (C) β23-tGFP-FUSZ-R/S. Cy3-labeled cEt PS-ASO (ION-598987) was transfected at 50 nM for 5 h (scale bars, 10 μm. Insert scale bars, 5 μm). (**D**) ROI-based image quantification of the granule/nuclear average pixel intensity of cEt PS-ASO in cells expressing β23-tGFP, β23-tGFP-FUSZ or β23-tGFP-FUSZ-R/S. For dot density plots, each data point represents one cell ($n = 16$ cells per group), and statistical analysis was performed using the Kruskal–Wallis one-way analysis of variance (* indicates $P < 0.01$). (**E**) Western blot analysis confirmed the expression of the recombinant proteins. Approximate molecular masses are noted at the right in kDa.

distribution of PS-ASO from both cytoplasmic and nuclear pools. Investigation of FUS binding to ASOs *in vitro* revealed the presence of at least two ASO binding sites within FUS: a higher affinity site formed by the LC and RRM domains and another site of slightly lower affinity formed by arginines within the C-terminal RGG domains. Similar to several PS-ASO binding proteins previously examined, FUS binds with higher affinity to ASOs containing the hydrophobic 2′ F and DNA modifications than to ASOs modified with MOE or cEt in the context of a PS backbone. Notably, the C-terminus of FUS fused to the artificial β-sheet protein β23 was sufficient to recruit cEt PS-ASO to cytoplasmic aggregates, whereas arginine-to-serine mutations within the same construct abrogated this phenotype. Although we do not exclude the possibility that ASO is attracted to β23-FUS-Z granules indirectly by additional FUS-Z interacting proteins, our findings support the hypothesis that high affinity PS-ASO binding proteins can influence the subcellular localization of PS-ASOs.

PS-ASO were previously reported to localize to nuclear paraspeckles that also contain P54nrb, PSF, FUS, and PSPC1. During transcriptional arrest, PS-ASOs delocalize with these proteins from paraspeckles to perinucleolar caps, suggesting that re-localization of proteins promotes the redistribution of PS-ASO (29,58,77). Additionally, nuclear enrichment of PS-ASOs can seed the formation of nuclear structures such as filaments containing P54nrb (29) and PS-bodies containing cytoplasmic protein TCP1β (26,78), suggesting that subcellular distributions of ASO-binding proteins can be altered due to interactions with PS-ASOs. In this study, we provided another example by showing that the expression of tGFP-FUS-P525L can redistribute pre-loaded PS-ASOs from the nucleus to cytoplasmic aggregates. This result also suggests that PS-ASO nuclear/cytoplasmic localization is dynamic and that the cytoplasmic RNP granules attract PS-ASOs from both nuclear and cytoplasmic pools.

Using semi-quantitative confocal image analysis, we examined the structural determinants of ASO localization to FUS granules and found that 5–10–5 gapmer cEt and LNA PS-ASOs were more efficiently enriched in FUS-P525L granules compared to the nucleus, whereas 2′ MOE, F and DNA PS-ASOs localized to both compartments. It is intriguing that cEt-modified PS-ASOs localized efficiently to cytoplasmic granules (Figure 6). Three different sequences as well as different fluorophores were tested in these experiments. We also observed a similar colocalization of FUS-P525L with LNA ASO. Previous work suggests that as the hydrophobicity of the 2′ modification increases PS-ASO binding to many (but not all) proteins is enhanced (25,26,28,29,31,32). It remains unclear why some hydrophobic 2′-modifications, such as 2′-F, bind to FUS and other proteins *in vitro* with higher affinity than does cEt, yet exhibit a more uniform localization between the nucleus and cytoplasmic granules (Figures 6–9, Supplementary Figure S10, (25,29,31,32)). It is possible that due to a generally higher affinity for proteins, 2′-F and 2′-DNA PS-ASOs are sequestered by abundant DNA/RNA binding proteins in the nucleus to a greater extent than is cEt PS-ASOs. It is also possible that FUS or other cytoplasmic RNP granule proteins have a higher capacity for binding cEt-modified PS-ASOs, which allows the recruitment of more cEt ASOs to the cytoplasmic RNP granule. Finally, the molecular self-structure within cEt or LNA PS-ASOs (79) may promote the assembly of cytoplasmic FUS aggregates or cytoplasmic FUS aggregates may promote cEt PS-ASO self-oligomerization. Indeed, fibrous multimeric assemblies of full-length FUS protein and of the FUS RGG-ZF-RGG domain alone can be seeded by RNA *in vitro* (67). Identification of individual proteins as well as protein structural features that confer selectivity for binding specific 2′ modifications will be of interest in future studies.

The nucleic acid binding properties of FUS have been the subject of numerous investigations, mostly with regard to its specificity for various nucleotide sequence motifs or RNA structures such as G-quadruplexes (57,65–67,80–87). Our previous data suggest that modifications, such as those to the sugar, alter ASO–protein interaction significantly. In addition, it appears that protein interactions with 2′-modified PS-ASOs can occur at sites other than those canonically bound by unmodified nucleic acids (25,28,31). In a competition experiment, we found that PS-DNA associated with FUS with an affinity more than 2500-fold higher than did the PO-DNA.

Our domain truncation studies examined how ASO chemical modifications influenced FUS binding to a single sequence (targeting the *PTEN* mRNA) and are largely in agreement with previous work. First, we and others (65,67) found that both the N- and C-terminal fragments of FUS, divided at the end of the RRM domain, bind nucleic acids, although we observed that FUS-NR binds PS-ASOs with approximately 2-fold higher affinity than FUS-Z (Figures 7, 9 and 10). A previous study found that FUS-N binds very weakly to PO RNA (67). We observed that FUS-N bound to MOE, cEt and F PS-ASOs, albeit with lower affinity than FUS-NR (Figure 7). The RGG repeats near the C-terminal end of FUS-N may interact more tightly with a phosphorothioate backbone than with a phosphodiester. Second, we and others detect very little nucleic acid binding by the FUS-RRM domain in isolation (66,86), consistent with a previously measured K_D of greater than 10 μM for PO RNA and DNA (83). Notably, we found that inclusion of additional N-terminal sequence adjacent to the RRM (called FUS-R1 in this report) significantly enhanced its binding affinity for PS-ASOs. Finally, our data indicate that the C-terminal RGG repeat domain, specifically the arginine residues therein, mediates the PS-ASO binding of FUS-Z to a considerable degree, whereas the zinc finger within FUS-Z provides only a marginal enhancement (Figures 8 and 10). Interestingly, it has been reported that aromatic amino acids (specifically F494 and F506) in this region contribute to the recognition of 2′-modifications within G-quadruplex structures (85,88,89), and this should be examined in the future with respect to PS-ASOs.

In summary, our results indicate that PS-ASOs, especially 5–10-5 gapmers with the cEt modification, can accumulate at a variety of cytoplasmic RNP granules including stress granules and granules seeded by the paraspeckle proteins FUS and PSF. Given the likelihood that interactions between PS-ASO and proteins mediate this phenotype, we performed a detailed characterization of the ASO binding sites within FUS and demonstrated that arginines

within the FUS-Z domain are sufficient to attract cEt PS-ASO to artificial β-sheet aggregates in cells. Our findings further the mechanistic understanding of ASO–protein interactions as well as the intracellular trafficking pathways relevant to ASO localization.

SUPPLEMENTARY DATA

Supplementary Data are available at NAR Online.

ACKNOWLEDGEMENTS

We wish to thank Timothy Vickers and Shiyu Wang for insightful discussions and technical advice.

FUNDING

Ionis Pharmaceuticals. Funding for open access charge: Ionis Pharmaceuticals.
Conflict of interest statement. None declared.

REFERENCES

1. Zamecnik,P.C. and Stephenson,M.L. (1978) Inhibition of Rous sarcoma virus replication and cell transformation by a specific oligodeoxynucleotide. *Proc. Natl. Acad. Sci. U.S.A.*, **75**, 280–284.
2. Bennett,C.F., Baker,B.F., Pham,N., Swayze,E. and Geary,R.S. (2017) Pharmacology of antisense drugs. *Annu. Rev. Pharmacol. Toxicol.*, **57**, 81–105.
3. Kole,R., Krainer,A.R. and Altman,S. (2012) RNA therapeutics: beyond RNA interference and antisense oligonucleotides. *Nat. Rev. Drug Discov.*, **11**, 125–140.
4. Crooke,S.T. (2007) *Antisense Drug Technology: Principles, Strategies, and Applications*, second edn. CRC Press.
5. Bauman,J., Jearawiriyapaisarn,N. and Kole,R. (2009) Therapeutic potential of splice-switching oligonucleotides. *Oligonucleotides*, **19**, 1–13.
6. Sazani,P. and Kole,R. (2003) Therapeutic potential of antisense oligonucleotides as modulators of alternative splicing. *J. Clin. Invest.*, **112**, 481–486.
7. Hua,Y., Vickers,T.A., Okunola,H.L., Bennett,C.F. and Krainer,A.R. (2008) Antisense masking of an hnRNP A1/A2 intronic splicing silencer corrects SMN2 splicing in transgenic mice. *Am. J. Hum. Genet.*, **82**, 834–848.
8. Chiriboga,C.A., Swoboda,K.J., Darras,B.T., Iannaccone,S.T., Montes,J., De Vivo,D.C., Norris,D.A., Bennett,C.F. and Bishop,K.M. (2016) Results from a phase 1 study of nusinersen (ISIS-SMN(Rx)) in children with spinal muscular atrophy. *Neurology*, **86**, 890–897.
9. Elkon,R., Ugalde,A.P. and Agami,R. (2013) Alternative cleavage and polyadenylation: extent, regulation and function. *Nat. Rev. Genet.*, **14**, 496–506.
10. Vorlova,S., Rocco,G., Lefave,C.V., Jodelka,F.M., Hess,K., Hastings,M.L., Henke,E. and Cartegni,L. (2011) Induction of antagonistic soluble decoy receptor tyrosine kinases by intronic polyA activation. *Mol. Cell*, **43**, 927–939.
11. Vickers,T.A., Wyatt,J.R., Burckin,T., Bennett,C.F. and Freier,S.M. (2001) Fully modified 2' MOE oligonucleotides redirect polyadenylation. *Nucleic Acids Res.*, **29**, 1293–1299.
12. Boiziau,C., Kurfurst,R., Cazenave,C., Roig,V., Thuong,N.T. and Toulme,J.J. (1991) Inhibition of translation initiation by antisense oligonucleotides via an RNase-H independent mechanism. *Nucleic Acids Res.*, **19**, 1113–1119.
13. Liang,X.H., Shen,W., Sun,H., Migawa,M.T., Vickers,T.A. and Crooke,S.T. (2016) Translation efficiency of mRNAs is increased by antisense oligonucleotides targeting upstream open reading frames. *Nat. Biotechnol.*, **34**, 875–880.
14. Wan,W.B. and Seth,P.P. (2016) The medicinal chemistry of therapeutic oligonucleotides. *J. Med. Chem.*, **59**, 9645–9667.
15. Geary,R.S., Norris,D., Yu,R. and Bennett,C.F. (2015) Pharmacokinetics, biodistribution and cell uptake of antisense oligonucleotides. *Adv. Drug Deliv. Rev.*, **87**, 46–51.
16. Stanton,R., Sciabola,S., Salatto,C., Weng,Y., Moshinsky,D., Little,J., Walters,E., Kreeger,J., DiMattia,D., Chen,T. *et al.* (2012) Chemical modification study of antisense gapmers. *Nucleic Acid Ther.*, **22**, 344–359.
17. Swayze,E. and Bhat,B. (2007) *Antisense Drug Technology*. CRC Press, pp. 143–182.
18. Janas,M.M., Jiang,Y., Schlegel,M.K., Waldron,S., Kuchimanchi,S. and Barros,S.A. (2017) Impact of oligonucleotide structure, chemistry, and delivery method on in vitro cytotoxicity. *Nucleic Acid Ther.*, **27**, 11–22.
19. Murray,S., Ittig,D., Koller,E., Berdeja,A., Chappell,A., Prakash,T.P., Norrbom,M., Swayze,E.E., Leumann,C.J. and Seth,P.P. (2012) TricycloDNA-modified oligo-2'-deoxyribonucleotides reduce scavenger receptor B1 mRNA in hepatic and extra-hepatic tissues–a comparative study of oligonucleotide length, design and chemistry. *Nucleic Acids Res.*, **40**, 6135–6143.
20. Kawasaki,A.M., Casper,M.D., Freier,S.M., Lesnik,E.A., Zounes,M.C., Cummins,L.L., Gonzalez,C. and Cook,P.D. (1993) Uniformly modified 2'-deoxy-2'-fluoro phosphorothioate oligonucleotides as nuclease-resistant antisense compounds with high affinity and specificity for RNA targets. *J. Med. Chem.*, **36**, 831–841.
21. Khvorova,A. and Watts,J.K. (2017) The chemical evolution of oligonucleotide therapies of clinical utility. *Nat. Biotechnol.*, **35**, 238–248.
22. Monia,B.P., Lesnik,E.A., Gonzalez,C., Lima,W.F., McGee,D., Guinosso,C.J., Kawasaki,A.M., Cook,P.D. and Freier,S.M. (1993) Evaluation of 2'-modified oligonucleotides containing 2'-deoxy gaps as antisense inhibitors of gene expression. *J. Biol. Chem.*, **268**, 14514–14522.
23. Watanabe,T.A., Geary,R.S. and Levin,A.A. (2006) Plasma protein binding of an antisense oligonucleotide targeting human ICAM-1 (ISIS 2302). *Oligonucleotides*, **16**, 169–180.
24. Geary,R.S. (2009) Antisense oligonucleotide pharmacokinetics and metabolism. *Expert Opin. Drug Metab. Toxicol.*, **5**, 381–391.
25. Liang,X.H., Sun,H., Shen,W. and Crooke,S.T. (2015) Identification and characterization of intracellular proteins that bind oligonucleotides with phosphorothioate linkages. *Nucleic Acids Res.*, **43**, 2927–2945.
26. Liang,X.H., Shen,W., Sun,H., Prakash,T.P. and Crooke,S.T. (2014) TCP1 complex proteins interact with phosphorothioate oligonucleotides and can co-localize in oligonucleotide-induced nuclear bodies in mammalian cells. *Nucleic Acids Res.*, **42**, 7819–7832.
27. Wang,S., Sun,H., Tanowitz,M., Liang,X.H. and Crooke,S.T. (2016) Annexin A2 facilitates endocytic trafficking of antisense oligonucleotides. *Nucleic Acids Res.*, **44**, 7314–7330.
28. Liang,X.H., Shen,W., Sun,H., Kinberger,G.A., Prakash,T.P., Nichols,J.G. and Crooke,S.T. (2016) Hsp90 protein interacts with phosphorothioate oligonucleotides containing hydrophobic 2'-modifications and enhances antisense activity. *Nucleic Acids Res.*, **44**, 3892–3907.
29. Shen,W., Liang,X.H. and Crooke,S.T. (2014) Phosphorothioate oligonucleotides can displace NEAT1 RNA and form nuclear paraspeckle-like structures. *Nucleic Acids Res.*, **42**, 8648–8662.
30. Krieg,A.M. and Stein,C.A. (1995) Phosphorothioate oligodeoxynucleotides: antisense or anti-protein? *Antisense Res. Dev.*, **5**, 241.
31. Vickers,T.A. and Crooke,S.T. (2016) Development of a quantitative BRET affinity assay for nucleic acid-protein interactions. *PLoS One*, **11**, e0161930.
32. Shen,W., Liang,X.H., Sun,H. and Crooke,S.T. (2015) 2'-Fluoro-modified phosphorothioate oligonucleotide can cause rapid degradation of P54nrb and PSF. *Nucleic Acids Res.*, **43**, 4569–4578.
33. Shang,Y. and Huang,E.J. (2016) Mechanisms of FUS mutations in familial amyotrophic lateral sclerosis. *Brain Res.*, **1647**, 65–78.
34. Yarosh,C.A., Iacona,J.R., Lutz,C.S. and Lynch,K.W. (2015) PSF: nuclear busy-body or nuclear facilitator? *Wiley Interdiscipl. Rev. RNA*, **6**, 351–367.
35. Knott,G.J., Bond,C.S. and Fox,A.H. (2016) The DBHS proteins SFPQ, NONO and PSPC1: a multipurpose molecular scaffold. *Nucleic Acids Res.*, **44**, 3989–4004.

36. Aulas,A. and Vande Velde,C. (2015) Alterations in stress granule dynamics driven by TDP-43 and FUS: a link to pathological inclusions in ALS? *Front. Cell Neurosci.*, **9**, 423.
37. Protter,D.S. and Parker,R. (2016) Principles and properties of stress granules. *Trends Cell Biol.*, **26**, 668–679.
38. Anderson,P. and Kedersha,N. (2008) Stress granules: the Tao of RNA triage. *Trends Biochem. Sci.*, **33**, 141–150.
39. Kedersha,N., Ivanov,P. and Anderson,P. (2013) Stress granules and cell signaling: more than just a passing phase? *Trends Biochem. Sci.*, **38**, 494–506.
40. Li,Y.R., King,O.D., Shorter,J. and Gitler,A.D. (2013) Stress granules as crucibles of ALS pathogenesis. *J. Cell Biol.*, **201**, 361–372.
41. Seyfried,N.T., Gozal,Y.M., Donovan,L.E., Herskowitz,J.H., Dammer,E.B., Xia,Q., Ku,L., Chang,J., Duong,D.M., Rees,H.D. *et al.* (2012) Quantitative analysis of the detergent-insoluble brain proteome in frontotemporal lobar degeneration using SILAC internal standards. *J. Proteome Res.*, **11**, 2721–2738.
42. Ramaswami,M., Taylor,J.P. and Parker,R. (2013) Altered ribostasis: RNA-protein granules in degenerative disorders. *Cell*, **154**, 727–736.
43. Shelkovnikova,T.A., Robinson,H.K., Southcombe,J.A., Ninkina,N. and Buchman,V.L. (2014) Multistep process of FUS aggregation in the cell cytoplasm involves RNA-dependent and RNA-independent mechanisms. *Hum. Mol. Genet.*, **23**, 5211–5226.
44. King,O.D., Gitler,A.D. and Shorter,J. (2012) The tip of the iceberg: RNA-binding proteins with prion-like domains in neurodegenerative disease. *Brain Res.*, **1462**, 61–80.
45. Dormann,D., Madl,T., Valori,C.F., Bentmann,E., Tahirovic,S., Abou-Ajram,C., Kremmer,E., Ansorge,O., Mackenzie,I.R., Neumann,M. *et al.* (2012) Arginine methylation next to the PY-NLS modulates Transportin binding and nuclear import of FUS. *EMBO J.*, **31**, 4258–4275.
46. Zhang,Z.C. and Chook,Y.M. (2012) Structural and energetic basis of ALS-causing mutations in the atypical proline-tyrosine nuclear localization signal of the Fused in Sarcoma protein (FUS). *Proc. Natl. Acad. Sci. U.S.A.*, **109**, 12017–12021.
47. Shelkovnikova,T.A., Peters,O.M., Deykin,A.V., Connor-Robson,N., Robinson,H., Ustyugov,A.A., Bachurin,S.O., Ermolkevich,T.G., Goldman,I.L., Sadchikova,E.R. *et al.* (2013) Fused in sarcoma (FUS) protein lacking nuclear localization signal (NLS) and major RNA binding motifs triggers proteinopathy and severe motor phenotype in transgenic mice. *J. Biol. Chem.*, **288**, 25266–25274.
48. Sharma,A., Lyashchenko,A.K., Lu,L., Nasrabady,S.E., Elmaleh,M., Mendelsohn,M., Nemes,A., Tapia,J.C., Mentis,G.Z. and Shneider,N.A. (2016) ALS-associated mutant FUS induces selective motor neuron degeneration through toxic gain of function. *Nat. Commun.*, **7**, 10465.
49. Sama,R.R., Ward,C.L., Kaushansky,L.J., Lemay,N., Ishigaki,S., Urano,F. and Bosco,D.A. (2013) FUS/TLS assembles into stress granules and is a prosurvival factor during hyperosmolar stress. *J. Cell Physiol.*, **228**, 2222–2231.
50. Schindelin,J., Arganda-Carreras,I., Frise,E., Kaynig,V., Longair,M., Pietzsch,T., Preibisch,S., Rueden,C., Saalfeld,S., Schmid,B. *et al.* (2012) Fiji: an open-source platform for biological-image analysis. *Nat. Methods*, **9**, 676–682.
51. Woerner,A.C., Frottin,F., Hornburg,D., Feng,L.R., Meissner,F., Patra,M., Tatzelt,J., Mann,M., Winklhofer,K.F., Hartl,F.U. *et al.* (2016) Cytoplasmic protein aggregates interfere with nucleocytoplasmic transport of protein and RNA. *Science*, **351**, 173–176.
52. Bolte,S. and Cordelieres,F.P. (2006) A guided tour into subcellular colocalization analysis in light microscopy. *J. Microsc.*, **224**, 213–232.
53. Jain,S., Wheeler,J.R., Walters,R.W., Agrawal,A., Barsic,A. and Parker,R. (2016) ATPase-modulated stress granules contain a diverse proteome and substructure. *Cell*, **164**, 487–498.
54. Buchan,J.R., Yoon,J.H. and Parker,R. (2011) Stress-specific composition, assembly and kinetics of stress granules in Saccharomyces cerevisiae. *J. Cell Sci.*, **124**, 228–239.
55. Dye,B.T. and Patton,J.G. (2001) An RNA recognition motif (RRM) is required for the localization of PTB-associated splicing factor (PSF) to subnuclear speckles. *Exp. Cell Res.*, **263**, 131–144.
56. Shelkovnikova,T.A., Robinson,H.K., Connor-Robson,N. and Buchman,V.L. (2013) Recruitment into stress granules prevents irreversible aggregation of FUS protein mislocalized to the cytoplasm. *Cell Cycle*, **12**, 3194–3202.
57. Sun,S., Ling,S.C., Qiu,J., Albuquerque,C.P., Zhou,Y., Tokunaga,S., Li,H., Qiu,H., Bui,A., Yeo,G.W. *et al.* (2015) ALS-causative mutations in FUS/TLS confer gain and loss of function by altered association with SMN and U1-snRNP. *Nat. Commun.*, **6**, 6171.
58. Shelkovnikova,T.A., Robinson,H.K., Troakes,C., Ninkina,N. and Buchman,V.L. (2014) Compromised paraspeckle formation as a pathogenic factor in FUSopathies. *Hum. Mol. Genet.*, **23**, 2298–2312.
59. Anderson,P. and Kedersha,N. (2002) Stressful initiations. *J. Cell Sci.*, **115**, 3227–3234.
60. Nishimoto,Y., Nakagawa,S., Hirose,T., Okano,H.J., Takao,M., Shibata,S., Suyama,S., Kuwako,K., Imai,T., Murayama,S. *et al.* (2013) The long non-coding RNA nuclear-enriched abundant transcript 1_2 induces paraspeckle formation in the motor neuron during the early phase of amyotrophic lateral sclerosis. *Mol. Brain*, **6**, 31.
61. Hennig,S., Kong,G., Mannen,T., Sadowska,A., Kobelke,S., Blythe,A., Knott,G.J., Iyer,K.S., Ho,D., Newcombe,E.A. *et al.* (2015) Prion-like domains in RNA binding proteins are essential for building subnuclear paraspeckles. *J. Cell Biol.*, **210**, 529–539.
62. West,J.A., Mito,M., Kurosaka,S., Takumi,T., Tanegashima,C., Chujo,T., Yanaka,K., Kingston,R.E., Hirose,T., Bond,C. *et al.* (2016) Structural, super-resolution microscopy analysis of paraspeckle nuclear body organization. *J. Cell Biol.*, **214**, 817–830.
63. Dammer,E.B., Fallini,C., Gozal,Y.M., Duong,D.M., Rossoll,W., Xu,P., Lah,J.J., Levey,A.I., Peng,J., Bassell,G.J. *et al.* (2012) Coaggregation of RNA-binding proteins in a model of TDP-43 proteinopathy with selective RGG motif methylation and a role for RRM1 ubiquitination. *PLoS One*, **7**, e38658.
64. Yang,C., Tan,W., Whittle,C., Qiu,L., Cao,L., Akbarian,S. and Xu,Z. (2010) The C-terminal TDP-43 fragments have a high aggregation propensity and harm neurons by a dominant-negative mechanism. *PLoS One*, **5**, e15878.
65. Wang,X., Schwartz,J.C. and Cech,T.R. (2015) Nucleic acid-binding specificity of human FUS protein. *Nucleic Acids Res.*, **43**, 7535–7543.
66. Bentmann,E., Neumann,M., Tahirovic,S., Rodde,R., Dormann,D. and Haass,C. (2012) Requirements for stress granule recruitment of fused in sarcoma (FUS) and TAR DNA-binding protein of 43 kDa (TDP-43). *J. Biol. Chem.*, **287**, 23079–23094.
67. Schwartz,J.C., Wang,X., Podell,E.R. and Cech,T.R. (2013) RNA seeds higher-order assembly of FUS protein. *Cell Rep.*, **5**, 918–925.
68. Eckstein,F. (2000) Phosphorothioate oligodeoxynucleotides: what is their origin and what is unique about them? *Antisense Nucleic Acid Drug Dev.*, **10**, 117–121.
69. Machleidt,T., Woodroofe,C.C., Schwinn,M.K., Mendez,J., Robers,M.B., Zimmerman,K., Otto,P., Daniels,D.L., Kirkland,T.A. and Wood,K.V. (2015) NanoBRET—a novel BRET platform for the analysis of protein-protein interactions. *ACS Chem. Biol.*, **10**, 1797–1804.
70. Giudice,G., Sanchez-Cabo,F., Torroja,C. and Lara-Pezzi,E. (2016) ATtRACT—a database of RNA-binding proteins and associated motifs. *Database (Oxford)*, **2016**, baw035.
71. Altmeyer,M., Neelsen,K.J., Teloni,F., Pozdnyakova,I., Pellegrino,S., Grofte,M., Rask,M.B., Streicher,W., Jungmichel,S., Nielsen,M.L. *et al.* (2015) Liquid demixing of intrinsically disordered proteins is seeded by poly(ADP-ribose). *Nat. Commun.*, **6**, 8088.
72. Vasilyev,N., Polonskaia,A., Darnell,J.C., Darnell,R.B., Patel,D.J. and Serganov,A. (2015) Crystal structure reveals specific recognition of a G-quadruplex RNA by a beta-turn in the RGG motif of FMRP. *Proc. Natl. Acad. Sci. U.S.A.*, **112**, E5391–E5400.
73. Thandapani,P., O'Connor,T.R., Bailey,T.L. and Richard,S. (2013) Defining the RGG/RG motif. *Mol. Cell*, **50**, 613–623.
74. Du,K., Arai,S., Kawamura,T., Matsushita,A. and Kurokawa,R. (2011) TLS and PRMT1 synergistically coactivate transcription at the survivin promoter through TLS arginine methylation. *Biochem. Biophys. Res. Commun.*, **404**, 991–996.
75. Tradewell,M.L., Yu,Z., Tibshirani,M., Boulanger,M.C., Durham,H.D. and Richard,S. (2012) Arginine methylation by PRMT1 regulates nuclear-cytoplasmic localization and toxicity of FUS/TLS harbouring ALS-linked mutations. *Hum. Mol. Genet.*, **21**, 136–149.
76. Olzscha,H., Schermann,S.M., Woerner,A.C., Pinkert,S., Hecht,M.H., Tartaglia,G.G., Vendruscolo,M., Hayer-Hartl,M., Hartl,F.U. and Vabulas,R.M. (2011) Amyloid-like aggregates sequester numerous metastable proteins with essential cellular functions. *Cell*, **144**, 67–78.

77. Bond,C.S. and Fox,A.H. (2009) Paraspeckles: nuclear bodies built on long noncoding RNA. *J. Cell Biol.*, **186**, 637–644.
78. Lorenz,P., Baker,B.F., Bennett,C.F. and Spector,D.L. (1998) Phosphorothioate antisense oligonucleotides induce the formation of nuclear bodies. *Mol. Biol. Cell*, **9**, 1007–1023.
79. Beane,R.L., Ram,R., Gabillet,S., Arar,K., Monia,B.P. and Corey,D.R. (2007) Inhibiting gene expression with locked nucleic acids (LNAs) that target chromosomal DNA. *Biochemistry*, **46**, 7572–7580.
80. Zinszner,H., Sok,J., Immanuel,D., Yin,Y. and Ron,D. (1997) TLS (FUS) binds RNA in vivo and engages in nucleo-cytoplasmic shuttling. *J. Cell Sci.*, **110**, 1741–1750.
81. Iko,Y., Kodama,T.S., Kasai,N., Oyama,T., Morita,E.H., Muto,T., Okumura,M., Fujii,R., Takumi,T., Tate,S. *et al.* (2004) Domain architectures and characterization of an RNA-binding protein, TLS. *J. Biol. Chem.*, **279**, 44834–44840.
82. Nguyen,C.D., Mansfield,R.E., Leung,W., Vaz,P.M., Loughlin,F.E., Grant,R.P. and Mackay,J.P. (2011) Characterization of a family of RanBP2-type zinc fingers that can recognize single-stranded RNA. *J. Mol. Biol.*, **407**, 273–283.
83. Liu,X., Niu,C., Ren,J., Zhang,J., Xie,X., Zhu,H., Feng,W. and Gong,W. (2013) The RRM domain of human fused in sarcoma protein reveals a non-canonical nucleic acid binding site. *Biochim. Biophys. Acta*, **1832**, 375–385.
84. Daigle,J.G., Lanson,N.A. Jr, Smith,R.B., Casci,I., Maltare,A., Monaghan,J., Nichols,C.D., Kryndushkin,D., Shewmaker,F. and Pandey,U.B. (2013) RNA-binding ability of FUS regulates neurodegeneration, cytoplasmic mislocalization and incorporation into stress granules associated with FUS carrying ALS-linked mutations. *Hum. Mol. Genet.*, **22**, 1193–1205.
85. Takahama,K., Takada,A., Tada,S., Shimizu,M., Sayama,K., Kurokawa,R. and Oyoshi,T. (2013) Regulation of telomere length by G-quadruplex telomere DNA- and TERRA-binding protein TLS/FUS. *Chem. Biol.*, **20**, 341–350.
86. Yoneda,R., Suzuki,S., Mashima,T., Kondo,K., Nagata,T., Katahira,M. and Kurokawa,R. (2016) The binding specificity of Translocated in LipoSarcoma/FUsed in Sarcoma with lncRNA transcribed from the promoter region of cyclin D1. *Cell Biosci.*, **6**, 4.
87. Reber,S., Stettler,J., Filosa,G., Colombo,M., Jutzi,D., Lenzken,S.C., Schweingruber,C., Bruggmann,R., Bachi,A., Barabino,S.M. *et al.* (2016) Minor intron splicing is regulated by FUS and affected by ALS-associated FUS mutants. *EMBO J.*, **35**, 1504–1521.
88. Takahama,K. and Oyoshi,T. (2013) Specific binding of modified RGG domain in TLS/FUS to G-quadruplex RNA: tyrosines in RGG domain recognize 2'-OH of the riboses of loops in G-quadruplex. *J. Am. Chem. Soc.*, **135**, 18016–18019.
89. Takahama,K., Miyawaki,A., Shitara,T., Mitsuya,K., Morikawa,M., Hagihara,M., Kino,K., Yamamoto,A. and Oyoshi,T. (2015) G-Quadruplex DNA- and RNA-specific-Binding proteins engineered from the RGG domain of TLS/FUS. *ACS Chem. Biol.*, **10**, 2564–2569.